Acoustical-Molecular Techniques for Magnetic Resonance Imaging

by

Bo Zhu

M.Eng., Electrical Engineering and Computer Science
Massachusetts Institute of Technology, 2008
S.B., Electrical Engineering
Massachusetts Institute of Technology, 2007

SUBMITTED TO THE HARVARD-MIT DIVISION OF HEALTH SCIENCES AND TECHNOLOGY IN PARTIAL FULFILLMENT OF THE REQUIREMENTS FOR THE DEGREE OF

DOCTOR OF PHILOSOPHY IN BIOMEDICAL ENGINEERING
AT THE
MASSACHUSETTS INSTITUTE OF TECHNOLOGY

FEBRUARY 2016

Signature of Author ..... Signature redacted
Department of Health Sciences and Technology
January 26, 2016

Certified by ..... Signature redacted
Bruce R. Rosen, MD, PhD
Director, MGH Athinoula A. Martinos Center for Biomedical Imaging
Professor of Radiology and Health Sciences and Technology
Thesis Supervisor

Accepted by ..... Signature redacted
Emery N. Brown, MD, PhD
Director, Harvard-MIT Program in Health Sciences and Technology
Professor of Computational Neuroscience and Health Sciences and Technology

Acoustical-Molecular Techniques for Magnetic Resonance Imaging

by

Bo Zhu

Submitted to the Harvard-MIT Division of Health Sciences and Technology
on Feb 1, 2016, in partial fulfillment of the
requirements for the degree of
DOCTOR OF PHILOSOPHY
IN BIOMEDICAL ENGINEERING

Magnetic resonance imaging (MRI) is a remarkably flexible diagnostic platform due to the variety of clinically relevant physical, chemical, and biological phenomena it can detect. In addition to the host of endogenous contrast mechanisms available, MRI functionality can be further extended by incorporating exogenous factors to attain sensitivity to new classes of indicators. Molecular imaging with targeted injectable contrast agents and MR elastography with externally delivered acoustic vibrations are two such advancements with increasing clinical significance. Conventionally employed separately, this work explores how exogenous components can interact cooperatively in imaging disease and may be combined to more accurately stage disease progression and generate novel mechanisms of MR contrast, using contrast agents and acoustic stimulation as model systems.

We imaged hepatic fibrosis in a rat model and found that collagen-binding paramagnetic contrast agents and shear wave MR elastography had partially uncorrelated staging abilities, due to the disease condition's differential timing of collagen production and its stiff cross-linking. This complementary feature enabled us to form a composite multivariate model incorporating both methods which exhibited superior diagnostic staging over all stages of fibrosis progression.

We then integrated acoustics and molecular-targeting agents at a deeper level in the form of a novel contrast mechanism, Acoustically Induced Rotary Saturation (AIRS), which switches "on" and "off" the image contrast due to the agents by adjusting the resonance of the spin-lock condition. This contrast modulation ability provides unprecedented clarity in identifying contrast agent presence as well as sensitive and quantitative statistical measurements via rapidly modulated block design experiments.

Finally, we extend the AIRS method and show preliminary results for Saturation Harmonic Induced Rotary Saturation (SHIRS), which detects the second harmonic time-oscillation of iron oxide nanoparticles' magnetization in response to an oscillating applied field around B_0. We also illustrate an exploratory method of selectively imaging iron oxide agents by diffusion kurtosis measures of freely diffusing water in solutions of magnetic nanoparticles.

Thesis Supervisor: Bruce R. Rosen

Title: Professor of Health Sciences and Technology, Professor of Radiology at Harvard Medical School

Acknowledgements

There are many people who I would like to thank, without whom this work and my path would not be possible. I would first like to thank my thesis supervisor Bruce Rosen, who has been an incredible advisor. In addition to deep scientific knowledge and insights he has imparted to me, his continual encouragement and support over the years have made my graduate career an exciting and joyous learning experience, through all the natural ups and downs of the research process. I would also like to thank my co-supervisor Lawrence Wald, who has shown me the ropes in the art of the physical experiment. I am also indebted to Peter Caravan and Alan Jasanoff, who have provided invaluable wisdom and guidance as my thesis committee members.

I thank all of my friends and community for their care and encouragement, especially during the more difficult times in my life. You all have given me more than you know. I am indebted in so many ways to my parents, who have instilled in me a lifelong curiosity and drive to excel, and have sacrificed much to provide the best for me. My brothers Ted and Tim, for whom in the past I sought to be a role model, are increasingly becoming great examples of maturity for me to follow, in many ways. Finally, I thank Selina, the constant joy of my life. You are a blessing I could never have imagined.

Contents

List of Figures

Chapter 1

Introduction

Magnetic Resonance Imaging (MRI) is a powerful investigative tool for clinicians and researchers to observe structure and function in living organisms. The image contrast associated with MRI is due to the response of excited water protons in the presence of external magnetic fields. The heterogeneity of this response over different tissues and physiological conditions generates biologically relevant contrast, which is useful for clinical diagnostic or biomedical research purposes.

Most forms of MR contrast are endogenous; although external energy is delivered into the subject by the main and gradient magnetic fields and radiofrequency (RF) pulses to prepare and sensitize the proton magnetization to certain physical conditions, the biologically relevant evolution of the magnetization is usually due to endogenous biological properties and processes such as molecular/macromolecular content (which influences T1 and T2 relaxation), water diffusion and flow, and blood oxygenation, among others. A great amount of research has been and continues to be done to find clever methods of interfacing the magnetic and RF fields with nuclear spin magnetization to enable sensitivity to new and interesting biological phenomena.

MR contrast can be generated in an exogenous manner by delivery of external matter or energy to perturb the spin magnetization for the purpose of interrogating a biologically relevant

condition or property. One of the most common forms of exogenous MR contrast are injected contrast agents, typically gadolinium-based molecules or magnetic nanoparticles that accumulate in a tissue region of interest and signal their presence by perturbing T1 or T2/T2* contrast, respectively. These agents are often functionalized with targeting peptides or antibodies to selectively enhance the regions of an MR image that contain a particular molecule or cell type.

In recent years, another form of exogenous MR contrast has gained widespread interest: delivery of external acoustic energy to generate elastographic contrast. An external acoustic driver coupled to the subject typically transfers vibrations in the form of shear waves in tissues. By estimating the spatial frequencies of the shear waves at each voxel, an elastogram can be reconstructed to reveal the local shear stiffness values (and potentially other mechanical viscoelastic measures) in tissues of interest. Because certain diseased tissues, particularly cancerous, fibrotic, or cystic tissues, often present changes in viscoelastic properties, MR elastography is becoming an increasingly relevant non-invasive diagnostic tool.

In this thesis, I explore how the exogenous aspects of molecular imaging and acoustic stimulation interact in imaging disease and can be combined to more accurately stage disease progression and generate novel mechanisms of MR contrast.

In Chapter 2, I investigate how effectively collagen-binding contrast agents and MR elastography interrogate liver fibrosis, first as separate techniques, and then as an integrated composite evaluation. Fibrosis is a natural candidate for exogenous contrast because thus far

endogenous MR measures dependent on T1 and water diffusion do not appear to correlate well with fibrosis and its progression. Both collagen-enhanced imaging and MR elastography are well suited to assess fibrosis because the disease is characterized by pathological increases in collagen production as well as cross-linking of collagen and elastin fibers, causing increased tissue stiffness.

After performing inversion recovery T1 quantification and phase contrast MR elastography simultaneously on rats with a diethylnitrosamine (DEN) treatment model of liver fibrosis over varying disease timepoints (8, 12, and 16 weeks), we found that the $\Delta R1$ values associated with collagen content was able to stage early fibrosis well, but not for moderate or late stages, and in an opposite manner, the shear stiffness values from MR elastography only accurately staged advanced fibrosis. This complementary staging outcome, which is supported at the molecular level by the differential timing of collagen production and its cross-linking, enabled us to form a composite multivariate linear model incorporating both $\Delta R1$ and shear stiffness scores; the resultant composite metric was shown to discriminate well at both the early and late stages of fibrosis.

In Chapter 3, I report a novel technique, Acoustically Induced Rotary Saturation (AIRS), which uses acoustic frequency mechanical stimulation to generate modulatable MR contrast from magnetic nanoparticle contrast agents. The acoustic perturbations induce oscillating relative motion between local water and the magnetic nanoparticles, resulting in the spin-locked water experiencing sinusoidally varying magnetic fields which under frequency-matched resonant conditions causes coherent rotation of the magnetization (and thus contrast modulation) as

dictated by the dynamics of the Bloch Equation. Furthermore, the acoustic drive can be externally modulated to turn the effect on and off, allowing sensitive and quantitative statistical comparison, as well as removal of confounding image background variations.

We demonstrate this concept in a phantom validation experiment, using piezoelectric actuators to generate vibrational displacements of iron oxide samples. We can observe a resonant behavior of the signal changes with respect to the acoustic frequency where iron oxide is present. We show that this effect stays approximately constant across acoustic frequency, and behaves monotonically over actuator displacement and contrast agent concentration. Most importantly, the resonant effect allowed us to generate block-design "modulation response maps" indicating the contrast agents' location, as well as positive contrast images with suppressed background signal. This contrast mechanism addresses the long-standing challenge of accurately detecting MR contrast agents in the presence of complex background tissue.

In Chapter 4, I illustrate two imaging techniques at the exploratory stage that expand upon the concepts of the previous chapters and show preliminary results. Instead of introducing acoustic-frequency mechanical vibrations to generate nanoparticle contrast, Saturation Harmonic Induced Rotary Saturation (SHIRS) sinusoidally shifts the main B0 field to oscillate the magnetization strength of the iron oxide particles, which produces a rotary saturation effect that can be detected at the second harmonic to avoid the confounding drive field at the fundamental drive frequency. We show preliminary contrast modulation results in a liquid phantom experiment. The potential advantage of this method over AIRS is that it more directly generates an oscillating nanoparticle-based magnetic field and would not require delivery of mechanical vibrational waves, which can

introduce an additional source of experimental error. Finally, I introduce a technique to selectively image magnetic nanoparticles based on the nanoscale non-Gaussian magnetic fields that water molecules experience in a field of magnetic nanoparticles during random walk diffusion. With Monte Carlo simulations and diffusion-weighted imaging of phantom samples with varying concentrations of iron oxide nanoparticles, I show preliminary results demonstrating a monotonic and nearly linear relationship between the non-Gaussian measure of kurtosis and magnetic nanoparticle concentration. Because the high nanoparticle field strengths and unique nanoscale spatial distribution of the nanoparticle fields are not found naturally elsewhere in the body, this technique shows potential for selectively imaging magnetic nanoparticles *in-vivo*.

Chapter 2

Molecular imaging and elastography for liver fibrosis staging

2.1 Introduction

Chronic liver disease is an increasingly prevalent cause of morbidity and mortality worldwide [1], and results from a wide range of factors such as viral hepatitis, excess alcohol consumption, diabetes, and metabolic dysfunction. Repeated injury to the liver from these conditions results in a fibrotic tissue repair response that replaces necrotic tissue with extracellular matrix scar, rich in fibrilliar collagen. If the underlying causes of disease are eliminated early enough, liver fibrosis may be regressed to less advanced stages or be fully reversed to normal architecture and function [2], but if left unchecked, fibrosis will often progress to cirrhosis, which significantly impairs liver function and is the 12th leading cause of death in the United States [3]. Therefore, accurate assessment of fibrosis stage and early detection of fibrosis, as well as monitoring its response to therapy, are vital clinical requirements for effective management of liver disease.

Liver biopsy is the gold standard in assessing liver fibrosis [4], although it suffers from many limitations including sampling error, inter-observer variability, and risk of complications; hospitalization is required in 1-5% cases of biopsy [5,6]. Even at advanced stages of fibrosis, large error rates in diagnosis of 33% have been reported [7]. Furthermore, repeated biopsies to evaluate disease progression or response to treatment are not ideal due to increased risk of

complication. Therefore, non-invasive strategies that can repeatedly measure fibrosis throughout the entire organ are advantageous and urgently needed.

MR elastography (MRE) has gained considerable interest in recent years as a clinically relevant method to assess fibrosis, although it has been reported to be most reliable at detecting advanced fibrosis and cirrhosis, during which portal hypertension, inflammation, and collagen cross-linking are some of the commonly acknowledged factors contributing to late-stage liver stiffening [8–10] .

More recently, another imaging advancement, a peptide-based Type I collagen specific MR probe, termed EP-3533, enabled the ability to image collagen levels *in-vivo* as a targeted T1 contrast agent. We had previously reported data with EP-3533, and demonstrated its utility in cardiac, pulmonary, and hepatic models of fibrosis [11–16] . In a recent study we showed that EP-3533 could accurately stage liver fibrosis [13] and was more sensitive than other conventional MRI measures such as water diffusion.

In order to compare and contrast the effectiveness of MRE and collagen imaging in assessing liver fibrosis, we concurrently performed the two techniques on diethylnitrosamine (DEN)-treated rats. We examined the effectiveness of these imagine methods for staging liver fibrosis progression, and explored whether there could be advantages in incorporating both techniques for further increased accuracy in staging fibrosis.

2.2 Methods

2.2.1 Animal model

All experiments were performed in accordance with the NIH Guide for the Care of Use of Laboratory Animals and were approved by the institution's animal care and use committee. Male Wistar rats (Charles River Laboratories, Wilmington, MA) were administered weekly doses of 100 mg/kg of diethylnitrosamine (DEN) for either 8, 12, or 16 weeks, to induce fibrosis at different stages (n = 6 for each time point). Controls (n=4 for each time point) received phosphate buffered saline (PBS). Animals were imaged approximately one week after the last injection to avoid acute effects of DEN.

2.2.2 EP-3533 probe

EP-3533 comprises a ten amino acid cyclic peptide conjugated to three gadolinium (Gd) moieties, and was synthesized as previously reported [11]. The peptide confers affinity for type I collagen and the Gd moieties provide strong signal enhancement (relaxivity = 48.4 $mM^{-1}s^{-1}$ at 1.4 T) [16].

2.2.3 MR Imaging protocol

Animals were anesthetized with isoflurane (1–2%) and placed in a specially designed cradle. The tail vein was cannulated for intravenous delivery of the contrast agent while the animal was positioned in the scanner. Imaging was performed at 1.5T using a clinical MRI scanner (Siemens Healthcare, Malvern, PA) with a custom-built solenoid coil. Each animal was placed within the solenoid coil in the supine position. A silver needle (disposable silver acupuncture needles,

0.20 x 48 mm; Asahi Medical Instrument Co., Kawaguchi, Saitama, Japan) was inserted through a gap in the solenoid coil and into the liver tissue through the anterior body wall, in a setup similar to that of [17] . An electromechanical driver attached to the other end of the needle generated longitudinal sinusoidal vibrations at 200 Hz (Fig. 2.3A).

Respiratory-gated, 3D inversion recovery images were acquired prior to and 45 minutes following the intravenous administration of EP-3533. A non-selective inversion pulse was used and images were acquired with inversion recovery times of 50, 100, 200, 250, 300, 400 and 1000 ms. Image acquisition parameters consisted of an echo time of TE = 2.44 ms, field of view FOV = 120 x 120 mm, matrix = 192 x 192 (0.625 mm in-plane resolution), slice thickness = 0.6 mm, and 36 image slices. The effective repetition time was dictated by the respiration rate through gating. In order to confirm proper delivery of contrast agent, Dynamic Contrast Enhancement spoiled gradient echo (SPGR) acquisitions were taken during a four-minute interval, starting one minute before prior to injection to measure baseline signal levels.

Doses of the contrast agent were given based on animal surface area at 7.26 nmol/cm^2. The surface area (SA) for each animal was estimated by the standard formula $SA = k\, W^{2/3}$ where W is the weight in grams and k is the Meeh constant, which empirically is determined to be approximately 9.5 in rats [18,19] .

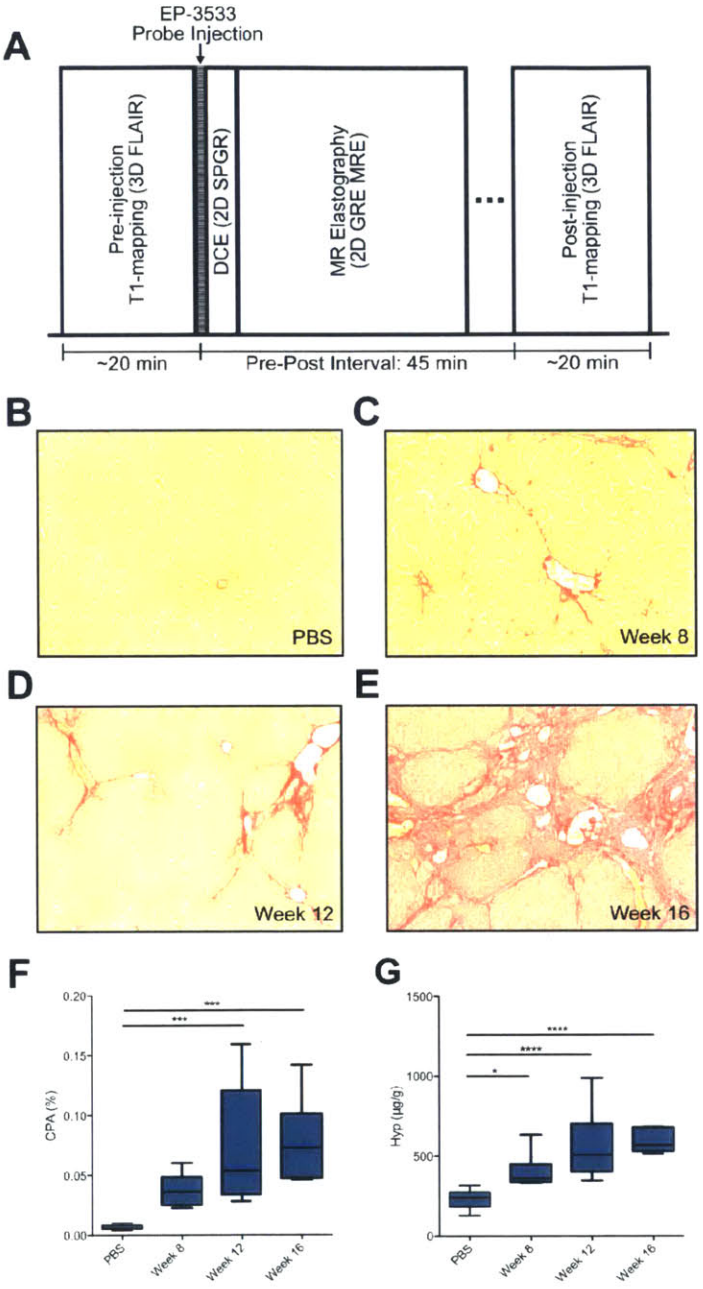

Fig. 2.1. Timing diagram of imaging experiment and characterization of DEN-induced rat model of liver fibrosis. (A) Timing diagram of imaging session, starting with a pre-injection inversion recovery sequence for T1 quantification, followed by EP-3533 probe injection, dynamic contrast enhancement to validate probe delivery to liver, MR elastography, and finally the post-injection inversion recovery acquisition 45 minutes after injection. (B-E) Representative images of Sirius Red staining after DEN administration for 8, 12, and 16 weeks. (F) Collagen proportional area as assessed by quantification of Sirius Red staining, increased progressively with time. (G) Total collagen as assessed by hydroxyproline analysis, increased progressively with time. * $p < 0.05$, ** $p < 0.01$, *** $p < 0.005$, and **** $p < 0.001$.

MR elastography of the rat liver was performed after the injection and DCE imaging, during the 45-minute pre-post interval. A gradient echo (GRE) MRE sequence was used for wave image acquisition with following parameters: matrix size 256x256, TR = 50 ms, TE = 23.3 ms, flip angle = 30°, slice thickness = 5 mm, field of view = 100mm x 100mm, one pair of 20 mT/m trapezoidal motion-encoding gradients (MEG) at 200 Hz. The trigger pulses initiating the sinusoidal oscillations of the electromechanical driver were moved relative to the MEG to obtain images at eight different phase offsets between the motion and the MEG, equally spaced over one cycle of the motion.

Following imaging, animals were sacrificed and liver tissue was subjected to pathologic scoring of fibrosis and analyzed for hydroxyproline content.

2.2.4 Postprocessing of MR Inversion Recovery data

T1 was quantified from a three parameter fit of the dependence of liver signal intensity (S) on inversion time (TI) and repetition time (TR) using a nonlinear least squares algorithm with a custom written MATLAB (Mathworks, Natick, MA) program.

$$S = S_0(1 - \cos\theta\, e^{-\frac{TR}{T_1}} - (1 - \cos\theta)e^{-\frac{TI}{T_1}}) \qquad \text{(Eq. 2.1)}$$

where S_0 is the signal intensity at full recovery, and θ is the flip angle. The liver signal intensity S is the averaged signal in regions of interest (ROIs) isolating the rat liver over a 2.4 mm-thick group of slices near the center of the liver.

The mean TR for each scan was extracted from the DICOM timestamp data by dividing the duration of the scan by the number of phase encode repetitions. Because the TR changes according to the respiratory rate of the animal, using the precise TR for each TI allows for more

accurate quantification of T1.

The difference between R1 (the inverse of T1) values between pre- and post- injection sessions were computed for each animal, and these ΔR1 values were then corrected based on the Gd concentration remaining in the blood, to account for variance between animals of probe delivery to the liver. This Gd concentration was extracted by T1 measurements of blood voxels.

2.2.5 Postprocessing of MR Elastography data

A phase gradient (PG) reconstruction method reported previously by Yin, et al. [17] was employed to extract shear stiffness values from the acquired data. For each animal, the phase of the first temporal harmonic of the acquired wave images were computed and unwrapped. The phase values along evenly-spaced spokes radially propagating from the needle location were selected to represent an aggregate phase gradient in the liver, which was derived by a linear fit of the phase values over radial distance. The phase gradient is directly related to the spatial wavelength ($\lambda = 2\pi/PG$), and this spatial wavelength is used to calculate the shear stiffness μ via the well-known elastic wave mechanics relation $\mu = f^2\lambda^2\rho$, where f is the temporal frequency of the shear wave vibration (in this case 200 Hz), and ρ is the density of the tissue, typically estimated in elastography experiments to be 1000 kg/m^3.

2.2.6 Generation of composite scoring metric

Multivariate analysis of variance (MANOVA) was performed on the ΔR1 and MRE data to form a single composite score based on linear combination of the two original metrics. Optimal linear weighting coefficients were determined such that the linear combination resulted in maximum discrimination between the Ishak groups according to the F-test statistic SS_B/SS_W, where SS_B is

the sum-of-squares between groups and SS_W is the sum-of-squares within groups [20]. MANOVA analysis was calculated from custom code in a MATLAB (Mathworks, Natick, MA) program.

2.2.7 Statistical analysis

Data are displayed as box plots with the dark band inside the box representing the mean, the bottom and top of the box the first and third quartiles, and the whiskers the minimum and maximum values. Data are reported as the mean ± standard error. Statistical analyses (Analysis of Variance (ANOVA) and Receiver Operating Characteristic (ROC) analysis) were performed using Prism 6 (GraphPad Software, Inc., La Jolla, CA) with $p < 0.05$ considered as significant. Differences among groups were tested with one-way ANOVA followed by the Tukey post-hoc test.

2.2.8 Tissue analysis

Formalin-fixed samples were embedded in paraffin, cut into 5 lm-thick sections and stained with Sirius Red according to standard procedures. Sirius Red stained sections were analyzed by a pathologist, who was blinded to the study, to score the amount of liver disease according to the method of Ishak. In addition, the collagen proportional area (CPA) was morphometrically calculated using ImageJ (NIH). Hydroxyproline in tissue was quantified by HPLC analysis as previously described [21]. Gd was quantified in tissue acid digests by inductively coupled plasma-mass spectrometry using dysprosium as an internal standard. Hydroxyproline and Gd are expressed as amounts per wet weight of tissue.

2.3 Results

2.3.1. Characterization of fibrosis disease progression

Liver fibrosis and disease progression in the DEN rat model was characterized by the CPA of histological tissue sections (Fig. 2.1B–E) and HPLC analysis of hydroxyproline content. CPA increased progressively at each time point from 0.69 ± 0.05% for PBS rats, 3.77 ± 0.56% for week 8 DEN rats, 7.32 ± 2.01% for week 12 DEN rats, to 7.83 ± 1.43 for week 16 rats (Fig. 2.1F). Hydroxyproline content also increased progressively with time from 229 ± 17 μg/g for PBS rats, 404 ± 47 μg/g for week 8 rats, 563 ± 92 μg/g for week 12 rats, and 591 ± 30 μg/g for week 16 rats (Fig. 2.1G).

2.3.2. Enhanced liver T1 shortening in DEN rats

A respiratory-gated, three-dimensional inversion recovery MRI sequence was used to quantify T1 of the liver. Representative inversion recovery images at TI = 400 ms for data acquired pre and post-EP3533 are shown in Fig. 2.2 for week 16 DEN rat (Fig. 2.2A and 2.2C) and a PBS control rat (Fig. 2.2B and 2.2D). A more dramatic signal enhancement is observed following contrast agent injection for the DEN rat compared to the PBS rat, which is indicative of increased T1 shortening due to greater accumulation of the EP-3533 contrast agent. This difference in T1 shortening is more precisely demonstrated by T1 fitting of acquired data at all TIs (Fig. 2.2E-F). The difference between the pre- (blue) and post-EP3533 (red) curves is greater for the DEN animal than for the control.

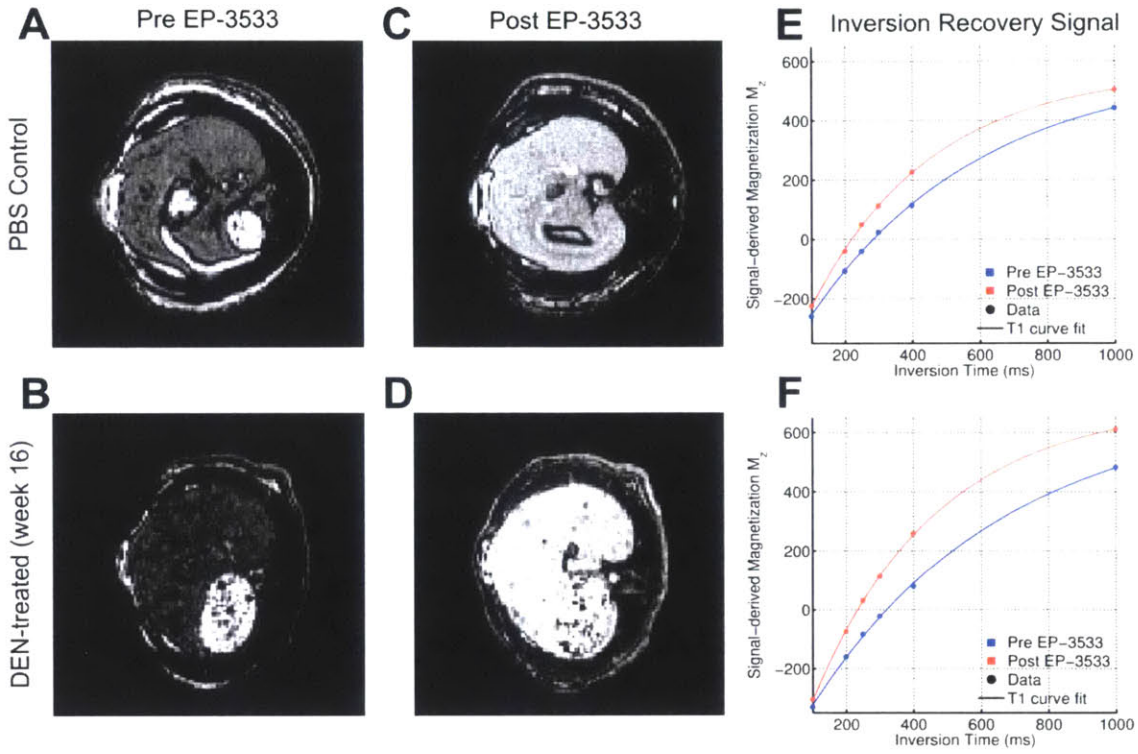

Fig. 2.2. T1 imaging and quantification of rat liver. (A,B) Pre-injection inversion recovery scans for PBS (A) and DEN-treated (B) rats at an inversion time of 400 ms. (C,D) Post-injection inversion recovery scans for PBS (C) and DEN-treated (D) rats at an inversion time of 400 ms. The signal enhancement is noticeably larger for the DEN-treated rats (B vs. D). (E-F) The signal averaged over liver ROI for all inversion times, with a T1 inversion recovery model (solid line) fitting the data (circles).

2.3.3 Increased liver shear stiffness in DEN rats

Shear stiffness measurements of the rat livers were taken by magnetic resonance elastography. Using a conventional local frequency estimation (LFE) method to post-process the MRE acquisitions yields elastograms such as those in Fig. 2.3C and 3D, which show representative elastograms of a PBS control rat liver and a week 16 DEN rat liver, respectively. Much greater shear stiffness values were observed in the DEN-treated rat liver than the control liver. Because hepatic fibrosis is typically distributed homogenously throughout the liver at the macroscopic scale [22] , it has been shown that highly precise measures of shear stiffnesses can be obtained

through phase gradient reconstruction of MRE acquisitions of radially propagating shear waves [17] . The higher spatial wavelengths observed in the radially propagating waves in the DEN liver (Fig. 2.3F) compared to that of the control (Fig. 2.3E) can be demonstrated quantitatively through this phase gradient method (Fig. 2.3G and 3H), whereby a single shear stiffness value representing the whole liver is extracted from the data with the analytical procedures previously described.

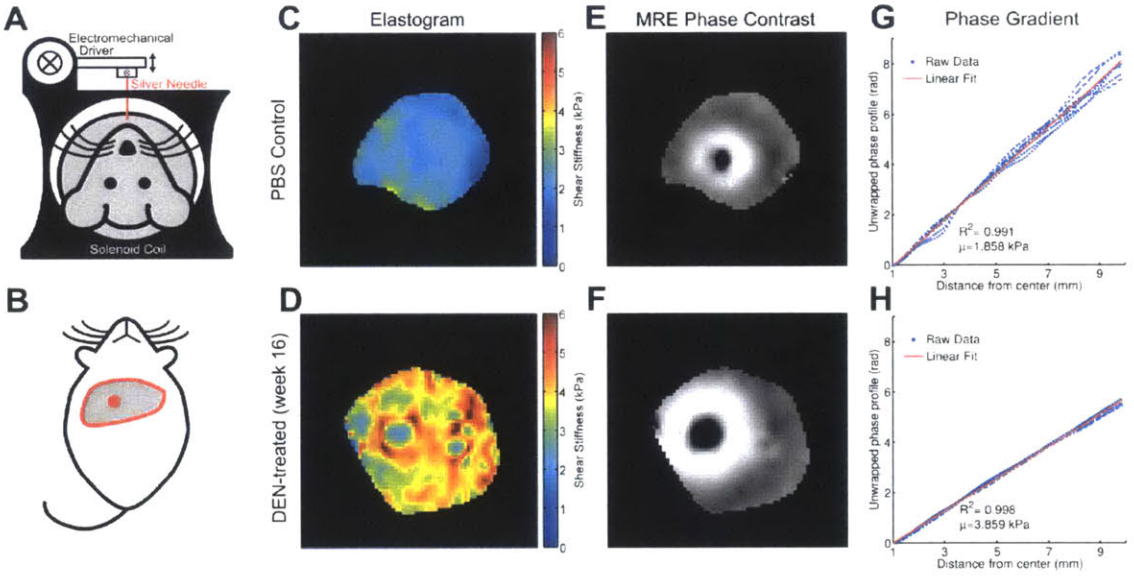

Fig. 2.3. MR elastography setup and phase gradient reconstruction of liver shear stiffness. (A) Experimental setup of vibration delivery. The rat is placed supine in the solenoid coil. Above, an electromechanical driver powered by an amplifier and signal generator (not illustrated) is connected to a silver acupuncture needle. (B) The needle is inserted into the rat liver which delivers vibrations from the driver directly into the liver tissue. (C-D) Conventional elastograms computed by local frequency estimation demonstrating greater shear stiffness in a DEN-treated animal (D) than in the PBS control (C). (E-F) Representative phase contrast images of shear waves radially propagating from the needle location. Note the greater spatial wavelengths in the DEN-treated animal (F), reflecting the greater shear stiffness. (G-H) The phase of the first temporal harmonic of these phase contrast images plotted over radial distance from the needle (blue) represents the phase gradient, which can be linearly fit (red) to quantify a shear stiffness value.

2.3.4 Fibrosis staging ability with ΔR1 and shear stiffness

To assess the ability of the techniques to stage liver fibrosis, we separated the animals into four groups based on Ishak score (Ishak 0, Ishak 1-2, Ishak 3-4, and Ishak 5-6) and CPA (CPA < 2%, CPA 2%-4%, CPA 4%-6%, and CPA > 6%). The CPA cutoffs were determined by its relationship to Ishak score: the CPA in all rats with Ishak 0 were below 2%, the majority of rats with Ishak 1-4 ranged from 2% to 4%, all rats with Ishak 5 ranged from 4%-6%, and all rats with Ishak 6 were above 6%. The ΔR1 and shear stiffness values for each group are plotted in Fig. 2.4. The general trend we observed was that the collagen probe (via ΔR1) exhibited the largest differences between the least fibrotic groups (Ishak 0 and CPA < 2%) and the other groups, while MRE (via shear stiffness) exhibited the largest differences between the most fibrotic groups (Ishak 5-6 and CPA > 6%) and the other groups. This complementary outcome is further supported by the symmetric nature of the statistically significant between-group differences displayed in Fig. 2.4.

Specifically, we observed that ΔR1 increased progressively with Ishak score, from 0.62 ± 0.02 s^{-1} for Ishak 0, 0.89 ± 0.05 s^{-1} for Ishak 1-2, 0.97 ± 0.05 s^{-1} for Ishak 3-4, to 1.09 ± 0.09 s^{-1} for Ishak 5-6. Statistically significant differences in ΔR1 were observed between Ishak 0 and Ishak 1-2 ($p < 0.05$), between Ishak 0 and Ishak 3-4 ($p < 0.01$), and between Ishak 0 and Ishak 5-6 ($p < 0.001$). Shear stiffness was observed to stay nearly constant from 2023 ± 124 Pa for Ishak 0, 2252 ± 242 Pa for Ishak 1-2, to 2103 ± 202 Pa for Ishak 3-4, until a large increase to 3894 ± 387 Pa for Ishak 5-6. Statistically significant differences in shear stiffness were observed between Ishak 0 and Ishak 5-6 ($p < 0.005$), between Ishak 1-2 and Ishak 5-6 ($p < 0.05$), and between Ishak 3-4 and Ishak 5-6 ($p < 0.05$). For the CPA groupings, we observed that ΔR1 increased from 0.62 ± 0.02 s^{-1} for CPA < 2% to 0.94 ± 0.03 s^{-1} for CPA 2%-4%, remained approximately

constant at 0.93 ± 0.08 s^{-1} for CPA 4%-6%, and increased to 1.12 ± 0.11 s^{-1} for CPA > 6%.

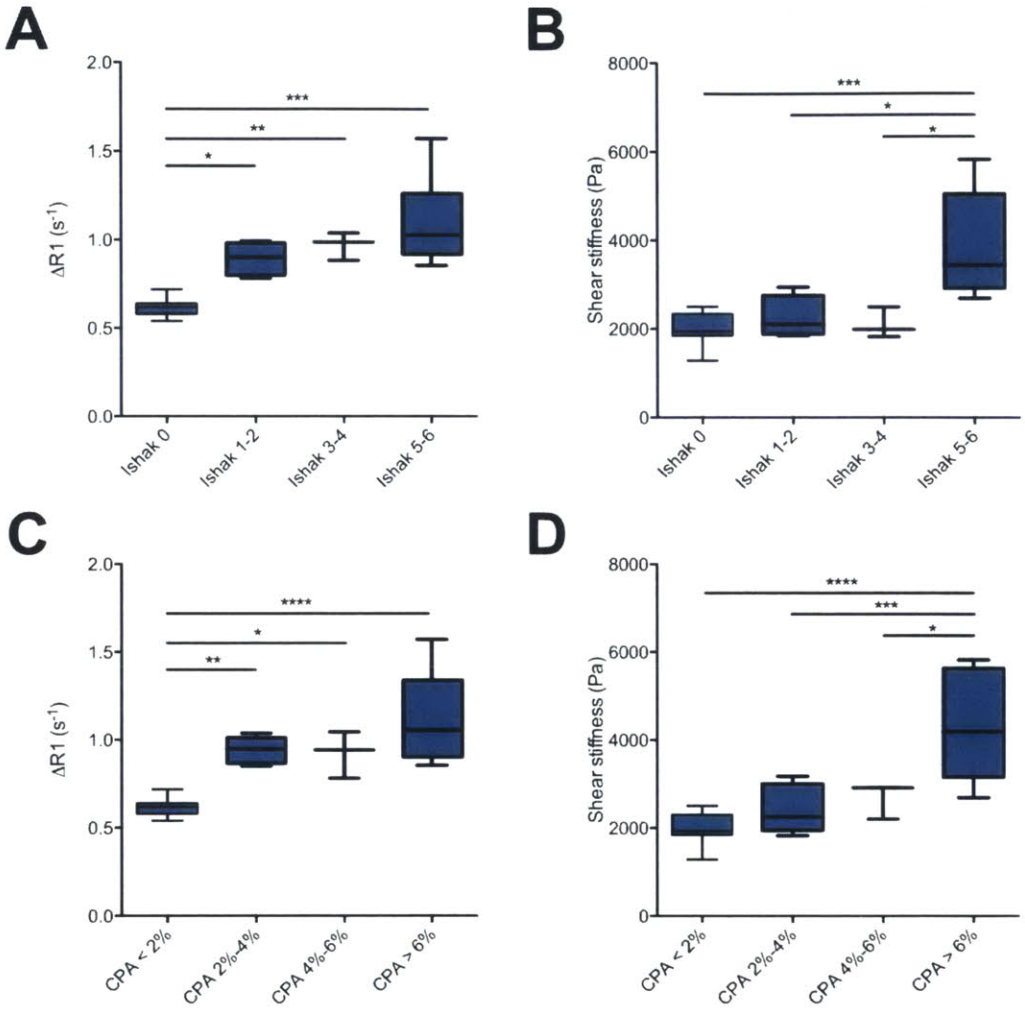

Fig. 2.4. Staging of liver fibrosis by collagen-enhanced MRI and MR elastography. Collagen-enhanced MRI is sensitive to early stages of fibrosis. ΔR1 significantly increases for fibrotic animals compared with non-fibrotic Ishak 0 (A) and CPA < 2% (C) animal groups. MR elastography is most sensitive to advanced stages of fibrosis. Shear stiffness significantly increases for the Ishak 5-6 (B) and CPA > 6% (D) groups compared with animals with less advanced fibrosis. The symmetric sensitivity of these methods indicate complementary staging capabilities. * $p < 0.05$, ** $p < 0.01$, *** $p < 0.005$, and **** $p < 0.001$.

Statistically significant differences in ΔR1 were observed between CPA < 2% and CPA 2%-4% ($p < 0.01$), between CPA < 2% and CPA 4%-6% ($p < 0.05$), and between CPA < 2% and CPA > 6% ($p < 0.001$). Shear stiffness was observed to be 2006 ± 112 Pa for CPA < 2%, 2252 ± 242 Pa for CPA 2%-4%, to 2103 ± 202 Pa for CPA 4%-6%, until a large increase to 3894 ± 387 Pa for

CPA > 6%. Statistically significant differences in shear stiffness were observed between CPA < 2% and CPA > 6% ($p < 0.001$), between CPA 2%-4% and CPA > 6% ($p < 0.005$), and between CPA 4%-6% and CPA > 6% ($p < 0.05$).

2.3.5 Fibrosis staging of ΔR1 and shear stiffness via ROC analysis

We also evaluated the effectiveness of these techniques to stage fibrosis by receiver operating characteristic (ROC) analysis. Using the same Ishak and CPA groups, the ROC analyses further support the complementary notion that collagen probe imaging is most suitable for differentiating non-fibrotic from fibrotic animals, while elastography is best for differentiating highly-fibrotic or cirrhotic animals from those with less advanced fibrosis; the highest area under the curve (AUC) for ΔR1 resulted from the comparison between non-fibrotic and fibrotic groups (Fig. 2.5A and 2.5G), and the highest AUC for shear stiffness resulted from the comparison between the most fibrotic group and the less fibrotic (including non-fibrotic) groups (Fig. 2.5F and 2.5L).

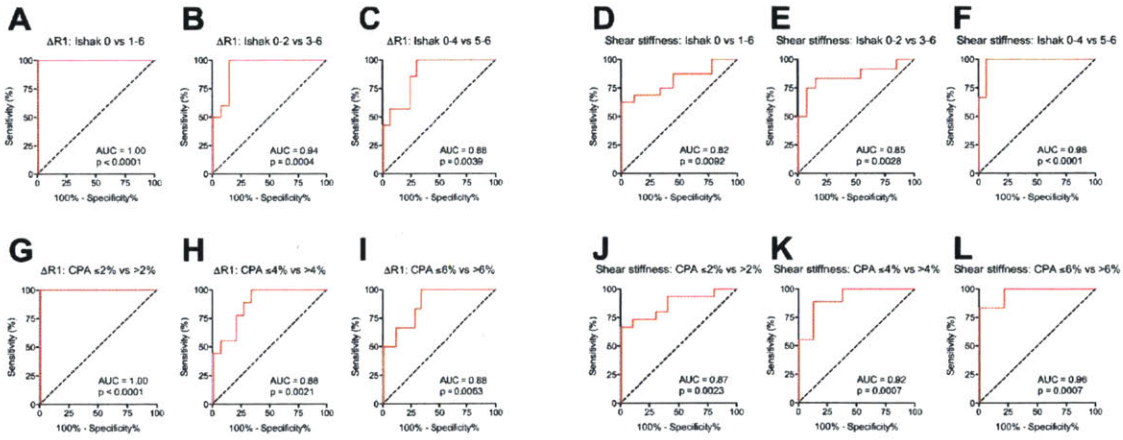

Fig. 2.5. Receiver operating characteristic (ROC) analysis of liver fibrosis staging by collagen-enhanced MRI and MR elastography. ROC curves are grouped by imaging technique and fibrosis metric: ΔR1 over Ishak stages (A-C) and CPA groups (G-I) and Shear stiffness over Ishak stages (D-F) and CPA groups (J-L). ROCs over both Ishak and CPA demonstrate collagen-enhanced MRI most suitable for discriminating early stages of fibrosis (decreasing AUC with fibrotic progression) while MR elastography most suitable for discriminating late stages of

fibrosis (increasing AUC with fibrotic progression) in this animal disease model.

The AUC for ΔR1 detecting fibrosis (Ishak 0 vs 1-6) was 1.00 (95% CI 1.00-1.00, $p < 0.0001$). The AUC for distinguishing early from significant fibrosis (Ishak 0-2 from Ishak 3-6) was 0.94 ± 0.05 (95% CI 0.83 to 1.00, $p = 0.0004$). Finally, the AUC for distinguishing significant to severe fibrosis (Ishak 0-4 from Ishak 5-6) was 0.88 ± 0.07 (95% CI 0.75 to 1.00, $p = 0.004$). Evaluated with CPA, the AUC for ΔR1 detecting fibrosis (CPA ≤ 2% vs > 2%) was 1.00 (95% CI 1.00-1.00, $p < 0.0001$). The AUC for distinguishing CPA ≤ 4% vs > 4% was 0.88 ± 0.07 (95% CI 0.75 to 1.00, $p = 0.0021$). Finally, the AUC for distinguishing CPA ≤ 4% vs > 4% was 0.88 ± 0.07 (95% CI 0.73 to 1.00, $p = 0.0063$).

By MR elastography, the AUC for shear stiffness detecting fibrosis (Ishak 0 vs 1-6) was 0.82 ± 0.08 (95% CI 0.66-0.98, $p = 0.0092$). The AUC for distinguishing early from significant fibrosis (Ishak 0-2 from Ishak 3-6) was 0.85 ± 0.08 (95% CI 0.69 to 1.00, $p = 0.0028$). Finally, the AUC for distinguishing significant to severe fibrosis (Ishak 0-4 from Ishak 5-6) was 0.98 ± 0.02 (95% CI 0.93 to 1.00, $p < 0.0001$). Evaluated with CPA, the AUC for MRE shear stiffness detecting fibrosis (CPA ≤ 2% vs > 2%) was 0.87 ± 0.07 (95% CI 0.73-1.00, $p < 0.0023$). The AUC for distinguishing CPA ≤ 4% vs > 4% was 0.92 ± 0.06 (95% CI 0.81 to 1.00, $p = 0.0007$). Finally, the AUC for distinguishing CPA ≤ 4% vs > 4% was 0.96 ± 0.04 (95% CI 0.89 to 1.00, $p = 0.0007$).

2.3.6 Multivariate composite scoring improves fibrosis staging

Because these two techniques were observed to have complementary staging abilities for detecting early (best with EP-3533 contrast agent imaging) and late stage fibrosis (best with MR elastography), we formulated a composite metric that accounted for both methods. We used

multivariate analysis of variance (MANOVA), an extended form of the generalized linear model (GLM), to form an optimal linear combination of the ΔR1 and shear stiffness values, resulting in a single composite score that yielded the greatest separation between the Ishak groups [20] . The MANOVA process decomposed the dataset into two canonical (or composite) variables, each of which are linear combinations of the original ΔR1 and shear stiffness values (Fig. 2.6A); CV1 = 8.02*R + 5.69*S - 7.06 and CV2 = -9.76*R + 3.92*S – 0.72, where CV1 and CV2 are the composite variables, R is the ΔR1 value in s^{-1} and S is the shear stiffness in kPa, and each linear combination is each subtracted by its mean. Composite Variable 1 represents the linear combination with maximum discrimination between Ishak groups, and when plotted in a conventional manner against Ishak groups (Fig. 2.6B), we observed this composite metric's ability to discriminate well between both early and late stage fibrosis.

This is further reflected by the ROC curves (Fig. 2.6C-E), which display superior AUC values compared to that determined by the individual ΔR1 and shear stiffness tests. The AUC for the composite score detecting fibrosis (Ishak 0 vs 1-6) was 1.00 (95% CI 1.00-1.00, $p < 0.001$). The AUC for distinguishing early from significant fibrosis (Ishak 0-2 from Ishak 3-6) was 0.96 ± 0.04 (95% CI 0.88 to 1.00, $p = 0.0001$). Finally, the AUC for distinguishing significant to severe fibrosis (Ishak 0-4 from Ishak 5-6) was 0.98 ± 0.03 (95% CI 0.93 to 1.00, $p = 0.0002$).

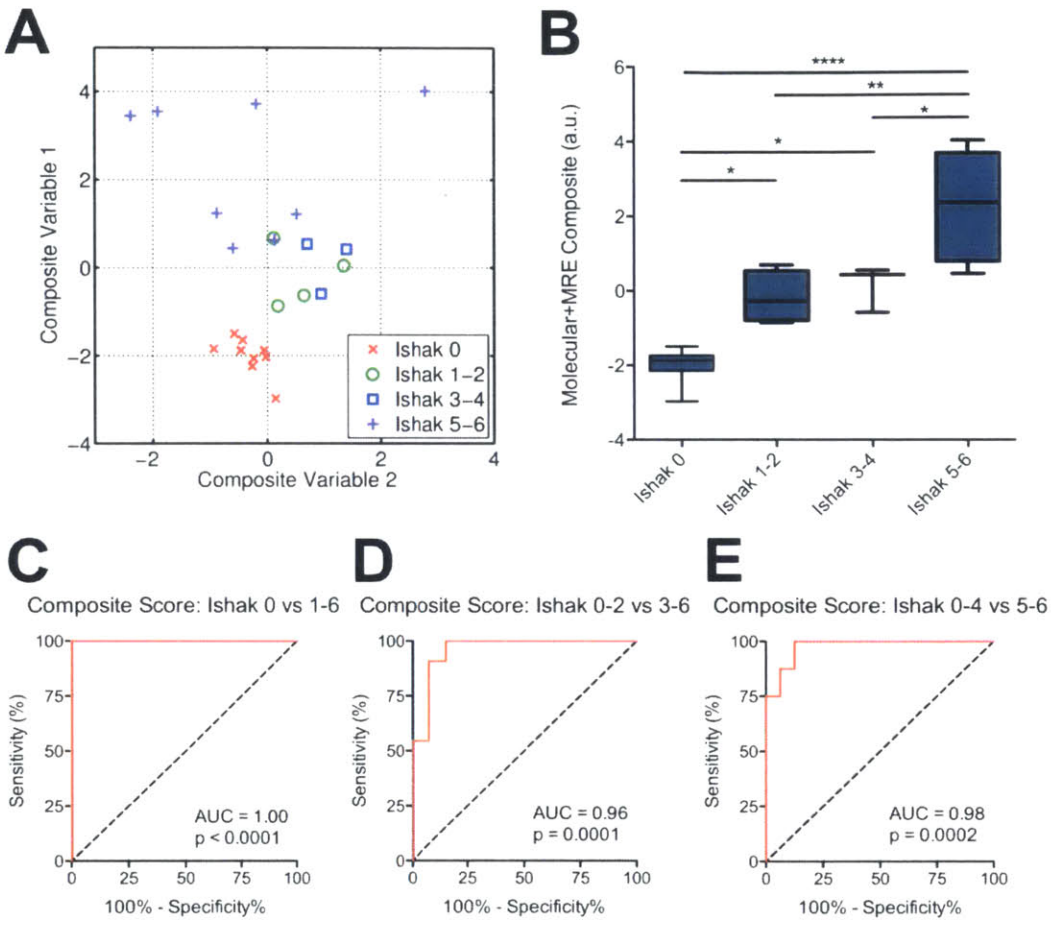

Fig. 2.6. Composite score for staging liver fibrosis incorporating collagen-enhanced imaging and MR elastography measures. (A) The ΔR1 and shear stiffness for each animal were linearly combined, with weighting coefficients optimized by multivariate analysis of variance (MANOVA) to achieve maximum separation between groups. The analysis generated two sets of coefficients, and the resultant linear combinations form Composite Variable 1 (with maximum separation) and Composite Variable 2 (with 2nd-highest separation). (B) Fibrosis staging by composite score (Composite Variable 1) incorporates the advantages of both imaging techniques and is capable of discriminating both early and late stages of fibrosis. (C-E) ROC curves demonstrating the composite score's ability to distinguish between fibrotic stage groups. These AUC values are the highest in comparison with those from Fig. 5, derived from the original imaging data. * $p < 0.05$, ** $p < 0.01$, and **** $p < 0.001$.

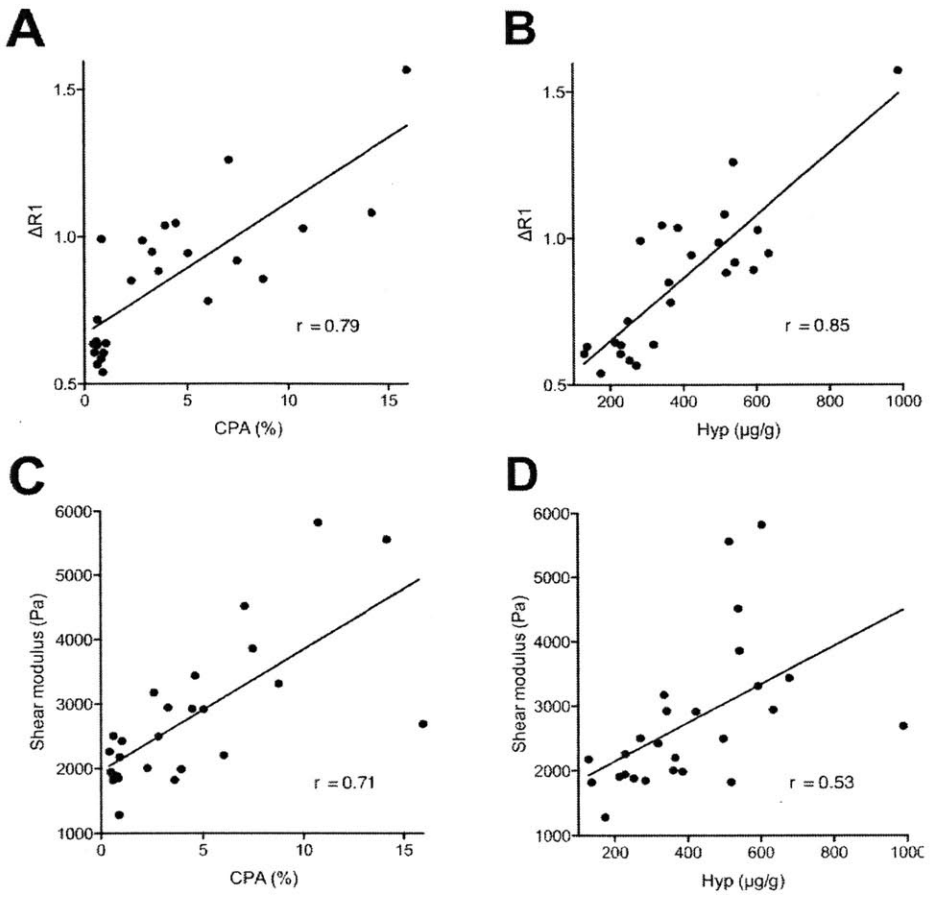

Fig. 2.7. ΔR1 and shear stiffness measurements over CPA and hydroxyproline concentration (A) Correlation between ΔR1 and CPA. (B) Correlation between ΔR1 and hydroxyproline content. (C) Correlation between shear modulus and CPA. (D) Correlation between shear modulus and hydroxyproline content.

2.4 Discussion

In this work we show for the first time simultaneous MR imaging of collagen content and tissue stiffness to compare and contrast each technique's ability to stage liver fibrosis in DEN-treated rats. Our results for each separate technique recapitulated previous findings for staging fibrosis. We observed the same exponential-like trend for tissue stiffness over fibrotic progression that has been widely reported in previous elastography literature [22,23] , resulting in good detection

for advanced fibrosis and cirrhosis, but not for earlier stages. Our previous EP-3533 studies also demonstrated the ability for the collagen probe to be sensitive in detecting early stages of fibrosis and reported similar AUC values in ROC analysis across discrimination stages [13,14].

An important consideration for diagnostic imaging is the relationship between the imaging measurement and the true biological condition the test is attempting to probe. Although MRE is conventionally a measurement of the elastic properties of tissue, confounds such as varying inflammation or perfusion levels (such as portal venous hypertension during cirrhosis) can influence the measurement. In fact, these are commonly cited contributors to the apparent late-stage increases in liver stiffness [24]. Similarly, molecular imaging is dependent upon pharmacokinetics, and perfusion characteristics of the tissue also affect probe delivery, which can obscure the desired measurement of molecular concentration. The early increases in $\Delta R1$ we observe are likely more reflective of the early collagen deposition during mild fibrosis, whereas decreased liver perfusion during the later stages of disease would likely decrease probe delivery and thus result in a flattening of the $\Delta R1$ values we observe.

Because these imaging techniques measure independent biophysical properties, the negative effects of these limitations may be ameliorated by using both techniques concurrently, especially in this study of fibrosis where we observe the complementary nature of these techniques in their ability to stage fibrosis. Again, the collagen-enhanced imaging was shown most effective in distinguishing non-fibrotic and early stages, and MR elastography most effective in distinguishing more advanced stages in this animal model.

By incorporating both measures, we generated a composite score model that was able to encapsulate both early and late-stage discrimination (AUROC > 0.96 for all comparisons) due to

the partially uncorrelated nature of the techniques. Although the specific coefficients of the model described here are tied to the exam parameters of this study (e.g. contrast agent dose, elastography frequency...), a multivariate collagen+MRE model can be instantiated for future experimental or clinical investigations by similar staging studies to determine optimal linear weighting coefficients.

The MR elastography reconstruction method we used was based on previous work [17] demonstrating the superior precision of the phase gradient technique in quantifying the shear stiffness value for predominately homogenously distributed diseases such as liver fibrosis. Although cirrhotic nodules at advanced stages may introduce focal perturbations of shear stiffness, the cirrhotic condition is already detectable by the bulk tissue stiffness, which we are more interested in. Additionally, the stiffness values of these small nodules are typically not accurately measured by MR elastography, especially in small animals where the spatial wavelengths of the shear waves are usually greater than the size of the nodules, because spatial frequency estimation is easily corrupted by noise in regions of interest (ROIs) with a low dynamic range of shear wave phase.

There were slight differences between this study and our previous EP-3533 staging study, with CCl4-treated mice demonstrated the ability to stage not only the non-fibrotic and mildly fibrotic stages, but also advanced fibrosis [13] . Since both this study and our previous study both had high linear correlations to hydroxyproline ($r=0.85$ and $r=0.89$, respectively), it is likely the staging discrepancy is due to differences in disease models that have differences in collagen deposition. Hydroxyproline levels were much higher in this study, and there were no Ishak 6 animals in the CCl4 study. Regardless, the ability for EP-3533 to be sensitive in detecting early stages of fibrosis is a consistent result across animal (rat vs. mouse) and disease (DEN-induced

vs CCl4-induced) models.

Prior literature reporting the direct elastic modulus measurements of fresh surgical samples of fibrotic liver corroborate our results, showing the elastic moduli at the lower fibrotic stages staying within similar ranges and only the highly fibrotic and cirrhotic livers with greater values [25] . One of the key molecular explanations suggested by literature is that cross-linking of collagen and elastin fibers, which has been shown to significantly increase tissue stiffness [26–28] , occurs typically in advanced fibrotic stages after initial collagen deposition [29–31] .

While elastography studies of patient populations with chronic liver diseases have typically shown similar results where insignificant stiffness differences are observed between non-fibrotic and mild fibrosis [22,23,32,33] , some recent studies, primarily small animal injury models with CCl4, have observed early-stage stiffness increases [10,24,34] even before fibrotic overproduction of collagen due to the cross-linking activity of lysyl oxidase. As many molecular mechanisms across varying models of fibrosis are still unresolved and under active investigation, one feature becoming increasingly apparent is that collagen production and the cross-linking that increases tissue stiffness have partially correlated but separate timelines that contribute differently to fibrotic progression. Therefore, we submit that imaging probes targeting collagen can provide useful information complementary to that of MR elastography toward the common goal of fibrosis staging, and models that incorporate both metrics can be advantageous in clinical and research settings.

Bibliography

[1] R. Williams, Global challenges in liver disease, Hepatology. 44 (2006) 521–526.

[2] Iredale, John P. "Models of liver fibrosis: exploring the dynamic nature of inflammation and repair in a solid organ." *Journal of Clinical Investigation*117.3 (2007): 539.

[3] SL Murphy, J Xu, KD Kochanek, Deaths: preliminary data for 2010., National Vital Statistics Reports: (2012) http://www.cdc.gov/nchs/products/nvsr.htm.

[4] Manning, Afdhal, Diagnosis and quantitation of fibrosis, Gastroenterology. 134:1670 – 1681 (2008).

[5] V Ratziu, F Charlotte, A Heurtier, S Gombert, P Giral, Sampling variability of liver biopsy in nonalcoholic fatty liver disease, Gastroenterology. 128:1898 –1906 (2005).

[6] Myers, Robert P., Andrew Fong, and Abdel Aziz M. Shaheen. "Utilization rates, complications and costs of percutaneous liver biopsy: a population-based study including 4275 biopsies." *Liver International* 28.5 (2008): 705-712.

[7] Afdhal, Nezam H., and David Nunes. "Evaluation of liver fibrosis: a concise review." *The American journal of gastroenterology* 99.6 (2004): 1160-1174.

[8] F. Vizzutti, U. Arena, R.G. Romanelli, L. Rega, M. Foschi, S. Colagrande, et al., Liver stiffness measurement predicts severe portal hypertension in patients with HCV related cirrhosis, Hepatology. 45 (2007) 1290–1297.

[9] M. Nakasaki, Y. Hwang, Y. Xie, S. Kataria, R. Gund, E. Hajam, et al., The matrix protein Fibulin-5 is at the interface of tissue stiffness and inflammation in fibrosis, Nat Commun. 6 (2015).

[10] Perepelyuk, Maryna, et al. "Hepatic stellate cells and portal fibroblasts are the major cellular sources of collagens and lysyl oxidases in normal liver and early after injury." *American Journal of Physiology-Gastrointestinal and Liver Physiology* 304.6 (2013): G605-G614.

[11] P. Caravan, B. Das, S. Dumas, F.H. Epstein, P.A. Helm, V. Jacques, et al., Collagen-Targeted MRI Contrast Agent for Molecular Imaging of Fibrosis, Angew Chem-Ger Edit. 119 (2007).

[12] M. Polasek, B. Fuchs, R. Uppal, D. Schühle, J. Alford, G. Loving, et al., Molecular MR imaging of liver fibrosis: A feasibility study using rat and mouse models, J Hepatol. 57 (2012).

[13] B.C. Fuchs, H. Wang, Y. Yang, L. Wei, M. Polasek, D.T. Schühle, et al., Molecular MRI of collagen to diagnose and stage liver fibrosis., J. Hepatol. 59 (2013) 992–8.

[14] Farrar, Christian T., Danielle K. DePeralta, Helen Day, Tyson A. Rietz, Lan Wei, Gregory Y. Lauwers, Boris Keil et al. "3D molecular MR imaging of liver fibrosis and response to rapamycin therapy in a bile duct ligation rat model."*Journal of Hepatology* (2015).

[15] Caravan, Peter, Yan Yang, Roshini Zachariah, Anthony Schmitt, Mari Mino-Kenudson, Howard H. Chen, David E. Sosnovik, Guangping Dai, Bryan C. Fuchs, and Michael Lanuti. "Molecular magnetic resonance imaging of pulmonary fibrosis in mice." *American journal of respiratory cell and molecular biology* 49, no. 6 (2013): 1120-1126.

[16] Helm, Patrick A., Peter Caravan, Brent A. French, Vincent Jacques, Luhua Shen, Yaqin Xu, Ronald J. Beyers, R. Jack Roy, Christopher M. Kramer, and Frederick H. Epstein. "Postinfarction Myocardial Scarring in Mice: Molecular MR Imaging with Use of a Collagen-targeting Contrast Agent 1." *Radiology*247, no. 3 (2008): 788-796.

[17] M. Yin, J. Woollard, X. Wang, V. Torres, P. Harris, C. Ward, et al., Quantitative assessment of hepatic fibrosis in an animal model with magnetic resonance elastography, Magn. Reson. Med. 58 (2007) 346–353.

[18] Gilpin, D. A. "Calculation of a new Meeh constant and experimental determination of burn size." *Burns* 22, no. 8 (1996): 607-611.

[19] Gouma, Simos, Verginadis, Lykoudis, Evangelou, Karkabounas, A simple procedure for estimation of total body surface area and determination of a new value of Meeh's constant in rats, Lab Anim-Uk. 46 (2012).

[20] Anderson, M.J., 2001. A new method for non-parametric multivariate analysis of variance. *Austral ecology*, *26*(1), pp.32-46.

[21] Hutson, Paul R., Mark E. Crawford, and Ronald L. Sorkness. "Liquid chromatographic determination of hydroxyproline in tissue samples." *Journal of Chromatography B* 791, no. 1 (2003): 427-430.

[22] Sandrin, L., Fourquet, B., Hasquenoph, J.M., Yon, S., Fournier, C., Mal, F., Christidis, C., Ziol, M., Poulet, B., Kazemi, F. and Beaugrand, M., 2003. Transient elastography: a new noninvasive method for assessment of hepatic fibrosis. *Ultrasound in medicine & biology*, *29*(12), pp.1705-1713.

[23] Ziol, Marianne, Adriana Handra-Luca, Adrien Kettaneh, Christos Christidis, Frédéric Mal, Farhad Kazemi, Victor de Lédinghen et al. "Noninvasive assessment of liver fibrosis by measurement of stiffness in patients with chronic hepatitis C." *Hepatology* 41, no. 1 (2005): 48-54.

[24] N. Salameh, B. Larrat, J. Abarca-Quinones, S. Pallu, M. Dorvillius, I. Leclercq, et al., Early detection of steatohepatitis in fatty rat liver by using MR elastography., Radiology. 253 (2009) 90–7.

[25] Yeh, Wen-Chun, Pai-Chi Li, Yung-Ming Jeng, Hey-Chi Hsu, Po-Ling Kuo, Meng-Lin Li, Pei-Ming Yang, and Po Huang Lee. "Elastic modulus measurements of human liver and correlation with pathology." *Ultrasound in medicine & biology* 28, no. 4 (2002): 467-474.

[26] Marturano, Joseph E., Joanna F. Xylas, Gautham V. Sridharan, Irene Georgakoudi, and Catherine K. Kuo. "Lysyl oxidase-mediated collagen crosslinks may be assessed as markers of functional properties of tendon tissue formation." *Acta biomaterialia* 10, no. 3 (2014): 1370-1379.

[27] Lau, Ying-Ka Ingar, Andre M. Gobin, and Jennifer L. West. "Overexpression of lysyl oxidase to increase matrix crosslinking and improve tissue strength in dermal wound healing." *Annals of biomedical engineering* 34, no. 8 (2006): 1239-1246.

[28] Elbjeirami, Wafa M., Edward O. Yonter, Barry C. Starcher, and Jennifer L. West. "Enhancing mechanical properties of tissue-engineered constructs via lysyl oxidase crosslinking activity." *Journal of Biomedical Materials Research Part A* 66, no. 3 (2003): 513-521.

[29] Friedman, Scott L. "Mechanisms of hepatic fibrogenesis." *Gastroenterology*134, no. 6 (2008): 1655-1669.

[30] Schuppan, Detlef, and Yong Ook Kim. "Evolving therapies for liver fibrosis."*The Journal of clinical investigation* 123, no. 123 (5) (2013): 1887-1901.

[31] Tzortzaki, Eleni G., Jay A. Tischfield, Amrik Sahota, Nikolaos M. Siafakas, Marion K. Gordon, and Donald R. Gerecke. "Expression of FACIT collagens XII and XIV during bleomycin-induced pulmonary fibrosis in mice." *The Anatomical Record Part A: Discoveries in Molecular, Cellular, and Evolutionary Biology* 275, no. 2 (2003): 1073-1080.

[32] Takahashi, Hirokazu, Naofumi Ono, Yuichiro Eguchi, Takahisa Eguchi, Yoichiro Kitajima, Yasunori Kawaguchi, Shunya Nakashita et al. "Evaluation of acoustic radiation force impulse elastography for fibrosis staging of chronic liver disease: a pilot study." *Liver international* 30, no. 4 (2010): 538-545.

[33] Sporea, Ioan, Roxana Şirli, Alina Popescu, Simona Bota, Radu Badea, Monica Lupşor, Mircea Focşa, and Mirela Dănilă. "Is it better to use two elastographic methods for liver fibrosis assessment?." *World journal of gastroenterology: WJG* 17, no. 33 (2011): 3824.

[34] Georges, Penelope C., Jia-Ji Hui, Zoltan Gombos, Margaret E. McCormick, Andrew Y. Wang, Masayuki Uemura, Rosemarie Mick, Paul A. Janmey, Emma E. Furth, and Rebecca G. Wells. "Increased stiffness of the rat liver precedes matrix deposition: implications for fibrosis." *American Journal of Physiology-Gastrointestinal and Liver Physiology* 293, no. 6 (2007): G1147-G1154.

Chapter 3

Selective Imaging of Magnetic Nanoparticles with Acoustically Induced Rotary Saturation

3.1 Introduction

Superparamagnetic iron oxide (SPIO) nanoparticles are widely used as contrast agents in magnetic resonance molecular imaging [1-3]. Due to the large susceptibility difference between injected SPIO nanoparticles and surrounding tissues, the presence of iron oxide nanoparticles can often be manually determined in T_2*-weighted images by darkened voxels due to the loss of MR signal around local field inhomogeneities induced by iron oxide. SPIO nanoparticles have been utilized in various contexts ranging from cancer imaging [4,5] to cell-tracking [6,7] to MR angiography [8,9].

3.1.1 Conventional challenges of locating iron oxide *in-vivo*

This manual SPIO locating process is problematic, given a complex tissue background having other naturally occurring regions of dark contrast (e.g., air or bone), as well as in regions with a low intrinsic signal-to-noise ratio (SNR). This long-standing practical challenge to the use of SPIO nanoparticle effectiveness as an *in-vivo* negative contrast agent has predominantly been addressed through acquisition and comparison of pre- and post- injection scans. Generally, however, these agents' slow biodistribution time, which requires a lengthy pre-post comparison interval, confounds this strategy. Subject motion, various forms of biological noise introduced

between scan sessions, and modulations in signal intensity corrupt comparison, making subtractive imaging and other quantitative pre-post comparison methods infeasible.

3.1.2 Recent contrast mechanism developments and their limitations

Recently, several techniques designed to increase the conspicuity of iron oxide contrast agents in MR acquisitions have been developed.

Off-resonance positive contrast imaging techniques typically use spectrally selective RF (SSRF) pulses to excite off-resonance spins susceptibility-shifted by the iron oxide nanoparticles [21] or suppress the on-resonance water with bandwidth-limited saturation [22]. The frequency range of excitation in these methods is best determined by prior knowledge of the concentration of the agent, which is often infeasible in *in-vivo* settings. These methods can also suffer from artifacts due to B_0 inhomogeneity, as the spins in the inhomogeneous fields with Larmor frequencies in the off-resonance passband become excited along with the iron oxide susceptibility-induced resonance shifts. Although B_0 field inhomogeneity also affects each spin-lock image acquisition with the AIRS technique, the artifacts that appear in both on- and off-resonance conditions disappear once the relative signal *change* between the conditions (caused only by B fields fluctuating at $\frac{\omega_{1lock}}{2\pi}$) is computed.

Positive contrast imaging with ultrashort echo time (UTE) sequences has also been demonstrated by subtracting an ultra-short echo time (e.g. 50 μs) acquisition and a longer echo time (e.g. 20 ms) acquisition, reversing the negative contrast due to T_2 decay [23,24]. However, this method is limited by potentially confounding subtractive contrast due to variations in the T_2 of background tissue.

3.1.3 Contrast modulation paradigm

Instead of contrast modulation from a one-time injection, a more desirable paradigm would be to repeatedly switch the contrast agent "on" and "off" in rapid succession; each k-space line (or single-shot image) could be acquired twice within seconds, and the resulting images would be compared (i.e. subtracted or subjected to a statistical test). This form of rapid comparison would be less sensitive to the low-frequency base-line intensity drift effects caused by motion, physiological noise, and instrumental drift.

3.1.4 Using Rotary Saturation to achieve contrast modulation

In this work, we describe a new contrast mechanism for selectively detecting iron oxide nanoparticle contrast agents, Acoustically Induced Rotary Saturation (AIRS), whereby a rotating frame resonance condition is established between spin-locked water magnetization and time-oscillating magnetic fields generated by acoustic-frequency vibration of contrast agents. We utilize the rotary saturation effect [10, 11] where the spin-locked magnetization is resonantly sensitive to oscillating fields at the frequency $\omega = \gamma B_{1lock}$. Previous related experiments have used variants of the rotary saturation effect to detect oscillating electrical currents for the purpose of neuronal current imaging [12,13]. In our method, we utilize the fact that the resonant frequency can be conveniently brought into the auditory frequency range, ideal for vibrating magnetic particles or tissues using external sound or mechanical vibration. The relative motion between the oscillating nanoparticles and the neighboring water causes the spin-locked water to experience an oscillating local magnetic field on-resonance with the rotating frame resonance condition which in turn causes a resonant rotation of the spin-locked magnetization away from the spin-lock field, exhibiting an image intensity change after the readout sequence. This resonant effect can be modulated "on" or "off" by adjusting either the vibration or the spin-lock

frequency to on- or off- resonance, or by turning on or off the acoustic stimulation. Either case allows consecutive acquisitions of a given k-space line or single-shot image to be acquired with and without the SPIO's contrast modulation.

We present results demonstrating the AIRS principle with a liquid phantom and characterize the effect of the vibration frequency, amplitude and contrast agent concentration. Furthermore, we show the ability to generate an fMRI-like activation map, hereby referred to as "modulation response map," of contrast agent presence through a functional imaging-type "block design" experiment where the effect of the contrast agent is cycled on and off. The rapid interleaving of on/off states is thus robust to the slowly varying modulations in image intensity, which confound conventional pre- and post- injection comparisons. The ability to detect contrast agents with a functional imaging model also allows quantifiable measurement of the contrast agent effect using well-established statistical analysis tools.

3.2 Theory

3.2.1 Spin-lock pulse sequence

During a spin-lock preparation sequence, a $90°_x$ excitation is first used to bring the magnetization vector M to $\hat{y}$ in the rotating frame of reference (rotating at the Larmor frequency). A spin-lock field B_{1lock} also rotating at the Larmor frequency is then applied along the $\hat{y}$ in the rotating frame. Since the only field present in the rotating frame ($B_{1lock}\hat{y}$) and the magnetization are co-linear, this field "locks" the rotating frame transverse magnetization along this axis. The rotating frame Larmor frequency ($\omega_{1lock} = \gamma B_{1lock}$) dictates the frequency needed for an external transverse field to alter the energy of the spin system in the locked state.

Thus, longitudinal relaxation ($T_{1\rho}$) in the spin-locked state is sensitive to external fields oscillating at γB_{1lock}.

3.2.2 Rotary Saturation

In the rotary saturation effect, the presence of a second field $B_{rotarysat}$ during spin-lock driven at or near the angular frequency γB_{1lock} will coherently rotate the magnetization away from the spin-lock axis [10- 12]. These rotating frame effects in response to fields oscillating at γB_{1lock} are therefore analogous to conventional RF excitation and T_1 relaxation, which occur, respectively, in response to coherent driving fields or intrinsic fluctuating fields oscillating near $\omega_0 = \gamma B_0$.

The dynamics of the phenomenon can be more conveniently understood in a doubly-rotating frame, which rotates around the spin-lock axis at a frequency ω_{1lock}. In this frame the applied field $B_{rotarysat}$ is stationary along the z axis. The equations of motion for the magnetization in the spin-lock condition within the doubly-rotating frame are presented with the y axis aligned along the spin-lock direction:

$$\frac{dM}{dt} = \gamma M \times \left[B_{1lock}\left(1 - \frac{\omega_{rotarysat}}{\gamma|B_{1lock}|}\right) + B_{rotarysat}\right] - R(M - M_p) \qquad \text{(Eq. 3.1)}$$

with

$$R = \begin{pmatrix} \frac{1}{T_2^*} & 0 & 0 \\ 0 & \frac{1}{T_{1\rho}} & 0 \\ 0 & 0 & \frac{1}{T_2^*} \end{pmatrix} \qquad \text{(Eq. 3.2)}$$

where intrinsic T_{2^*} and $T_{1\rho}$ relaxations occur in accordance with the rotating frame equilibrium magnetization M_ρ.

An important aspect of the Rotary Saturation effect is that its effect on the magnetization is narrowband. The magnetization undergoes rotation in the doubly-rotating frame only when $\omega_{rotarysat}$ and ω_{1lock} are matched, due to the excitation analogy mentioned above. This resonant feature is illustrated in Fig. 3.1, and can be obtained quantitatively in the solution for Equations 3.1 and 3.2.

Previous experiments demonstrated the Rotary Saturation effect with rotary saturation fields $B_{rotarysat}$ generated by coils outside solid and liquid samples [11] and wire current dipoles in liquid phantoms [12,13]. In our method, the rotary saturation field, $B_{rotarysat}$ is generated by the vibrating iron oxide contrast agents themselves.

3.2.3 Rotary Saturation field by oscillating magnetic particles

An accumulation of magnetic nanoparticles in a static homogenous $\boldsymbol{B_0}$ field exhibits a magnetic field perturbation approximated by that of a magnetized sphere, as described in [14]:

$$\Delta B_z(r,\theta) = \frac{\Delta\chi B_0}{3}\left(\frac{a}{r}\right)^3 (3\cos^2\theta - 1), \qquad \text{(Eq. 3.3)}$$

where $\Delta\chi$ is the difference in bulk magnetic susceptibility between the sphere and the surroundings, a is the sphere radius, r is the distance to the center of the sphere, and θ is the angle between r and B_0.

For small sinusoidal displacements of a magnetic nanoparticle cluster, an approximately sinusoidally time-varying field is generated. Consider a spherical iron oxide nanoparticle cluster

with field perturbation as previously described in Eq. 3.3: $\Delta B_z(r,\theta) = \frac{\Delta\chi B_0}{3}\left(\frac{a}{r}\right)^3 (3\cos^2\theta - 1)$.

In Cartesian coordinates, this becomes:

$$\Delta B_z(x,y,z) = \frac{\Delta\chi B_0}{3}\left(\frac{a}{\sqrt{x^2+y^2+z^2}}\right)^3 \left(\frac{3z^2}{x^2+y^2+z^2} - 1\right) \quad \text{(Eq. 3.4)}$$

The field at any point (x_0, y_0, z_0) can be approximated as linear in z for small excursions about (x_0, y_0, z_0). Consider a small time-varying displacement $\Delta z(t) \ll a$ of the nanoparticle cluster, where a is the sphere radius. For any point outside the nanoparticle cluster, $r > a$, the new magnetic field perturbation can be characterized with linear approximation around the operating point (x_0,y_0,z_0) by:

$$\Delta B_z(x,y,z,t) \approx \Delta B_z(x_0,y_0,z_0) + \left.\frac{d\Delta B_z}{dz}\right|_{(x_0,y_0,z_0)} \cdot \Delta z(t) \quad \text{(Eq. 3.5)}$$

For sinusoidal displacements $\Delta z(t) = \Delta z\, sin(\omega t)$, after substitutions and differentiation, we obtain:

$$\Delta B_z(x,y,z,t) \approx C_1 + C_2 \Delta z \sin(\omega t) \quad \text{(Eq. 3.6)}$$

where C_1 and C_2 are constants:

$$C_1 = \frac{\Delta\chi B_0}{3}\left(\frac{a}{\sqrt{x_0{}^2+y_0{}^2+z_0{}^2}}\right)^3 \left(\frac{3z_0{}^2}{x_0{}^2+y_0{}^2+z_0{}^2} - 1\right), \quad \text{(Eq. 3.7)}$$

$$C_2 = \frac{\Delta\chi B_0 a^3}{3}\frac{9x_0{}^2z_0+9y_0{}^2z_0-6z_0{}^3}{(x_0{}^2+y_0{}^2+z_0{}^2)^{7/2}} \quad \text{(Eq. 3.8)}$$

We observe the time-varying component of ΔB_z to be sinusoidal. Thus, for small sinusoidal displacements of a magnetic nanoparticle cluster, an approximately sinusoidally time-varying field is generated.

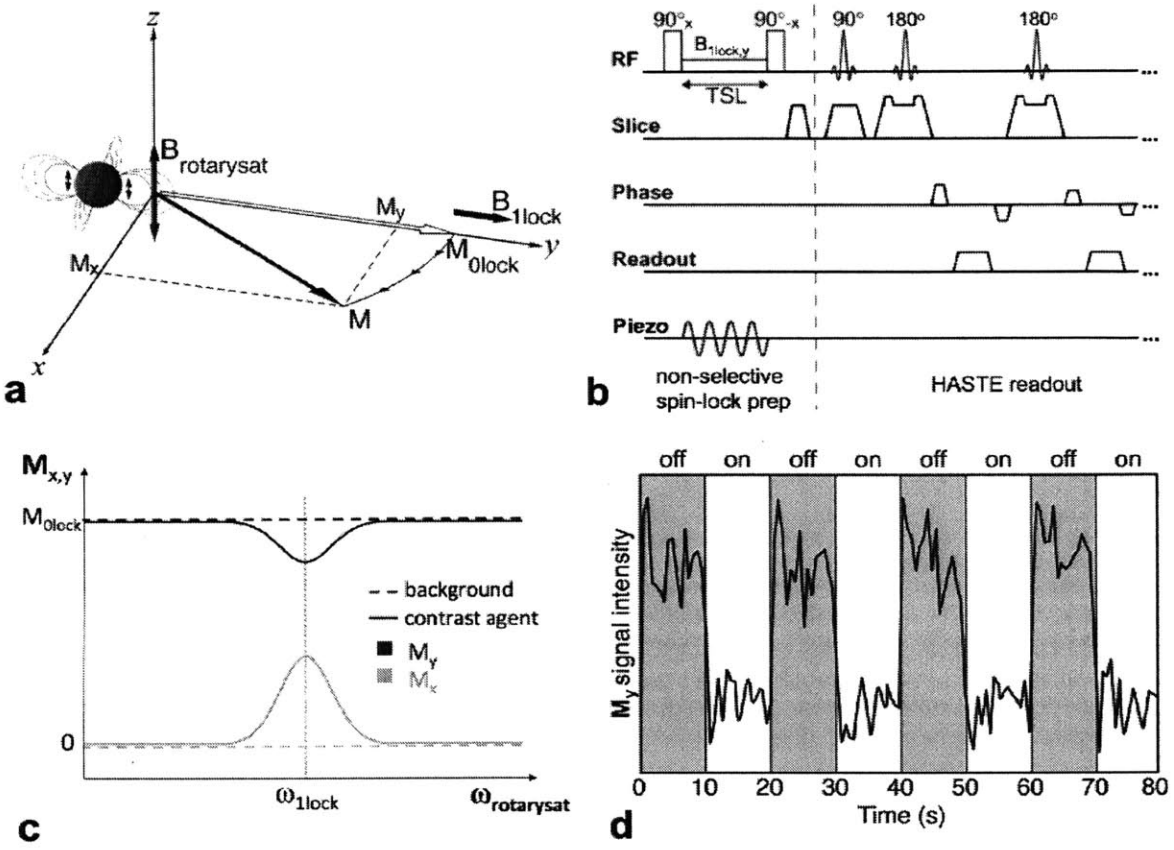

Fig. 3.1. Schematic representation of the method, ignoring relaxation. (a) After a 90° excitation, a rotary saturation field B_{1lock} is applied to spin lock the magnetization along the y axis, resonantly sensitizing the magnetization M (initially locked to M_{0lock}) to magnetic fields $B_{rotarysat}$ oscillating at a frequency γB_{1lock}. Iron oxide nanoparticles can be vibrated to generate this $B_{rotarysat}$ experienced by the local water and produce a resonant rotation of the magnetization M_{0lock} away from the y axis. (b) The pulse sequence is comprised of a spin-lock period, during which the iron oxide sample is vibrated by a piezoelectric actuator. The 90° pulse flips back either M_x or M_y to the z axis for imaging by a HASTE readout. The choice of whether to readout the x or y component of M is set by the phase of the flip-back 90° pulse. (c) The expected response of the measured M_x or M_y component (generating positive or negative contrast, respectively) as the frequency of the sample vibration $\omega_{acoustic}$ (and thus rotary saturation field $\omega_{rotarysat}$) is swept through the resonance condition ($\omega_{rotarysat} = \gamma B_{1lock}$). (d) The expected intensity variation in the vicinity of the contrast agent as the sample vibrations are switched between on- and off-resonance conditions. The block-design response is similar to that of functional imaging and can be analyzed by similar statistical methods yielding an fMRI-like activation map indicating the presence of the magnetic nanoparticle contrast agent (see Fig. 3.2d).

Our method uses this contrast agent-derived approximately sinusoidal field as the rotary saturation field $B_{rotarysat}$, causing a nutation of the magnetization M in voxels near the contrast agents when its frequency $\omega_{rotarysat}$ is near the spin-lock resonant frequency ω_{1lock} (Fig. 3.1a).

3.2.4 Positive or negative contrast via flipback pulse direction

At the end of the spin-lock preparation the magnetization is flipped to $\hat{z}$ by the choice of either a $90°_{-x}$ or $90°_{y}$ followed by a transverse spoiler, consequently returning either the M_y (by $90°_{-x}$) or M_x (by $90°_{y}$) component for subsequent imaging (Fig. 3.1b). The M_y component encodes the resonant AIRS effect as a signal loss as the magnetization is nutated away from $\hat{y}$, while the M_x component encodes the effect as a signal gain. For small nutation angles, M_x (which behaves according to the sine of the angle) will experience a larger effect than M_y (which behaves according to the cosine of the angle) (Fig. 3.1c). Choosing the M_x component will also result in a positive contrast image, because M_x grows during the rotation while the unperturbed background magnetization stays along $\hat{y}$ with no $\hat{x}$ component. In either case, the signal intensity depends upon the strength of the rotary saturation field, which is correlated with contrast agent concentration.

3.2.5 Block design experiment from resonance condition switching

Furthermore, the signal is frequency-dependent due to the rotary saturation resonance condition, and thus selective contrast can be obtained by comparing the signal between resonant ($\omega_{rotarysat} = \omega_{1lock}$) and non-resonant states ($\omega_{rotarysat} \neq \omega_{1lock}$) with an fMRI-like block design experiment, interleaving on-resonance and off-resonance acquisition blocks (Fig. 3.1d). By comparing the signal change between conditions across all image voxels, we interrogate the

strength of this effect spatially and generate a modulation response map with statistical methods utilized in functional imaging analyses.

3.3 Methods

3.3.1 Liquid phantom experimental setup

Experiments were performed in a spherical phantom (10 cm diameter) filled with a solution of 0.52 ml of Gadopentetate dimeglumine (Magnevist, Berlex Laboratories) yielding a T_1 measured by inversion recovery of 400 ms. Two NMR spherical bulb microcells (Wilmad 18μL spherical microcell inserts, Wilmad-LabGlass), one containing various concentrations of 10 nm Fe_2O_3 nanoparticles (Fe concentration = 200 μg/ml), and the other containing Fomblin® Perfluoropolyether (PFPE) oil (Solvay Chemicals), a control fluid with low signal and little susceptibility difference from the phantom solution, were lowered vertically into the liquid phantom. The microcells are composed of a 3 mm inner-diameter, 5 mm outer-diameter glass spherical shell, where the sample is contained, adjoined to a 0.9 mm inner-diameter, 1.1 mm outer-diameter glass capillary tube. The top of each glass tube (extending out from the phantom opening) was attached by epoxy to a piezoelectric bender actuator driven by a piezoelectric amplifier (T220-A4-203X model actuator and EPA-104-115 amplifier, Piezo Systems Inc, Woburn MA). Driven with an audio frequency function generator, the piezo induces vertical displacements of the samples oscillating in time at a chosen frequency $\omega_{acoustic}$. Because of the relationship previously described between the rotary saturation field and the vibrating contrast agent sample, $\omega_{rotarysat} = \omega_{acoustic}$. The displacements were calibrated and measured with laser doppler vibrometry. A third stationary microcell filled with the identical iron oxide

concentration was also lowered into the phantom to provide a second control to demonstrate the effect's dependence upon properly tuned vibrational motion.

3.3.2 MR pulse sequence

A spin-lock prepared single-shot HASTE pulse sequence (Fig. 3.1b) was used in a 1.5T scanner (Siemens Avanto, Siemens Healthcare, Erlangen Germany) to capture images with 256x256 matrix, 12-cm FOV, 5mm slice thickness, TE of 14 ms, and TR of 3.0 s. The piezoelectric sinusoidal actuations are gated to be active only within the 100 ms spin-lock preparation sequence, during which the magnetization is manipulated due to the rotary saturation phenomenon and subsequently imaged with the HASTE readout.

3.3.3 Block design experiment

To generate the modulation response map to indicate contrast agent presence, a block design experiment was conducted by acquiring a set of 100 single-shot HASTE images while switching resonance states (on-resonance: $\omega_{1lock} = \omega_{rotarysat}$, off-resonance $\omega_{1lock} \neq \omega_{rotarysat}$) in 20 image blocks. In our experiment, $\frac{\omega_{1lock}}{2\pi}$ = 75 Hz, and $\frac{\omega_{acoustic}}{2\pi} = \frac{\omega_{rotarysat}}{2\pi}$ switched between 75 Hz and 50 Hz. The iron oxide sample Fe concentration was 200 μg/ml and vibrated sinusoidally with peak-to-peak displacement amplitude 250 μm.

To generate a modulation response map, voxel-by-voxel analysis of the signal changes between on and off resonance states was carried out using standard fMRI methods; FEAT (FMRI Expert Analysis Tool) Ver. 5.98, in FSL (FMRIB's Software Library, www.fmrib.ox.ac.uk/fsl). Time-series statistical analysis was performed using FILM (FMRIB's Improved Linear Model) and contrasts were cluster corrected at threshold of $Z > 2.3$ ($p < 0.05$).

3.3.4 Characterization experiments

The strength of the AIRS effect in the liquid phantom setup was studied as a function of Fe concentration, nanoparticle sample vibration displacement amplitude, and nanoparticle sample vibration frequency. The contrast agent samples used in these characterization experiments were contained in cylindrical capillary tubes (1.1 mm inner-diameter, 1.3 mm outer-diameter, Fisher Scientific). The average image intensity values in a 2 mm radius ROI centered at the contrast agent location were obtained in both on-resonance ($\omega_{1lock} = \omega_{rotarysat}$) and off-resonance ($\omega_{1lock} = \omega_{rotarysat} + \Delta\omega$) conditions, where $\frac{\Delta\omega}{2\pi}$ was 25 Hz. The signal change $\Delta S/S$, was computed as the on-resonance to off-resonance signal difference over the off-resonance signal intensity. The Fe concentration in the samples were varied between 0 μg/ml (control) and 200 μg/ml (0 μg/ml, 50 μg/ml, 100 μg/ml, 150 μg/ml, 200 μg/ml) with $\frac{\omega_{rotarysat}}{2\pi}$ = 75 Hz and displacement 500 μm. Vibration peak-to-peak amplitude was varied between 10 μm and 500 μm (10 μm, 20 μm, 50 μm, 80 μm, 100 μm, 200 μm, 300 μm, 400 μm, 500 μm) with a 200 μg/ml Fe concentration sample and $\frac{\omega_{rotarysat}}{2\pi}$ = 50 Hz. The AIRS effect on contrast agent vibration frequency $\frac{\omega_{acoustic}}{2\pi}$ was studied at 50 Hz, 100 Hz, 150 Hz, and 200 Hz, with a vibrational displacement of 150 μm and 200 μg/ml Fe concentration sample and ω_{1lock} swept in intervals of 2Hz between 24 Hz below and 24 Hz above each $\frac{\omega_{acoustic}}{2\pi}$ value to form rotary saturation spectra.

Bloch simulation was performed to corroborate the relative changes in linewidth and peak intensities of the rotary saturation spectra across $\frac{\omega_{acoustic}}{2\pi}$ resonant frequencies. The time-evolution of the magnetization during the 100 ms spin-locked preparation according to the modified doubly-rotating frame Bloch equations (Eqs. 3.1-2) was simulated with a MATLAB

code solver with parameters T_1 = 395 ms, T_2 = 316 ms, T_2* = 46 ms, $T_{1\rho}$ was taken from the R2=1/T2 and R1=1/T1 values using the equation $T_{1\rho}$=2/(R2+R1) (10), and $B_{rotarysat}$ derived from the magnetic field perturbation of a cylindrical accumulation of iron oxide nanoparticles (14): $\Delta B_z(\rho,\varphi) = \frac{\Delta\chi B_0}{2}\left(\frac{a}{\rho}\right)^2 (2\cos^2\varphi - 1)$ in cylindrical coordinates, where the difference in bulk magnetic susceptibility difference between the cylinder and the surroundings $\Delta\chi = 1.5\times10^{-5}$, the cylinder radius $\boldsymbol{a}$ = 0.55mm, and the distance to the center of the cylinder $\boldsymbol{\rho}$= 2mm.

3.3.5 Positive contrast experiments

Extending the AIRS method to enable positive contrast imaging, the 90° flipback direction after the spin-lock preparation was switched to be along $\hat{y}$, resulting in signal growth for voxels near the contrast agent due to M_x being the component to be subsequently imaged, as detailed in the theory section. With 200 μg/ml samples in the liquid phantom setup with bulb samples, vibrated with a peak-to-peak amplitude of 150 μm and at $\frac{\omega_{acoustic}}{2\pi} = 75\ Hz$, we acquired 50 images on-resonance ($\frac{\omega_{1lock}}{2\pi} = 75\ Hz$) and 50 images without vibration for reference, primarily to remove the effect of B_0 field inhomogeneity manifesting as a signal confound. The reference images were subtracted from the on-resonance images and averaged over time to produce the final positive contrast image. We then performed statistical analysis on the voxel signal changes between on-resonance and no-vibration groups using the FSL FEAT and FSL FILM methods described above with the same parameters, obtaining modulation response maps to further validate the location of the vibrating contrast agent sample. We also studied the intensity of the positive contrast signal, averaged over a 4 mm radius ROI centered at the contrast agent location, as a function of Fe concentration at 50 μg/ml, 100 μg/ml, 75 μg/ml, 100 μg/ml, 150 μg/ml, and 200 μg/ml samples.

3.4 Results

3.4.1 Liquid phantom block design experiment

The essential capabilities of the AIRS method are demonstrated in Fig. 3.2. Fig. 3.2b shows a conventional T_2-weighted image of the liquid phantom setup and demonstrates the limitation that similarly hypointense contrast sources appear undifferentiated; the iron oxide samples cannot be distinguished from the fluorinated oil sample. As the block design experiment proceeds through on-resonance and off-resonance acquisition blocks, the signal intensity is modulated in voxels near the vibrating contrast agent sample, as shown by the single voxel signal intensity timeseries in Fig. 3.2c. The modulations in signal intensity clearly match the timing of the switches between on/off -resonance states. These signal modulations can be observed particularly clearly in the sequence of raw images acquired during the block design experiment.

To generate a modulation response map, voxel-by-voxel statistical analysis of the signal changes between on and off resonance states was carried out using standard fMRI GLM analysis methods. Fig. 3.2d shows the highest z scores corresponding to voxels in proximity to the vibrated contrast agent sample, demonstrating the selective contrast agent detection capability of the AIRS contrast mechanism. Some residual contrast appearing near the fluorinated oil sample is likely primarily due to differences in turbulent motion between the two vibration settings that introduce slightly different T_2^* shortening during the acquisitions.

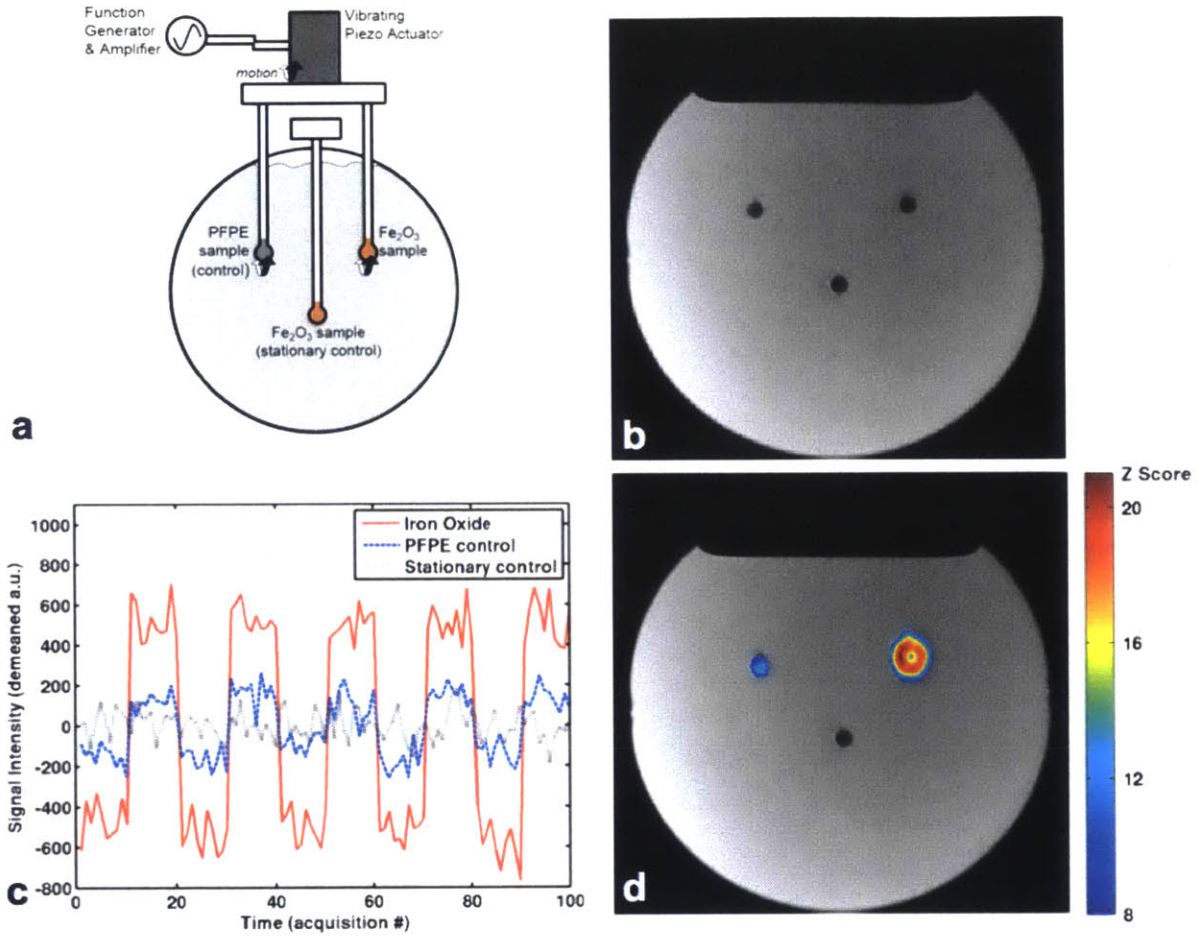

Fig. 3.2. Liquid phantom validation experiment. (a) A spherical Gd-doped H_2O solution phantom contains three glass spherical bulbs; two contain aqueous Fe_2O_3 samples and one contains Fomblin PFPE oil. The Fomblin and Fe_2O_3 samples are simultaneously vibrated by piezoelectric drive while the other Fe_2O_3 acts as a stationary control. (b) A conventional T_2-weighted coronal slice acquisition showing all three samples as undifferentiated hypointense regions. (c) Time course of voxel intensities near each sample over the duration of the block-design experiment where interleaved blocks of on-resonance (acoustic drive and spin-lock frequency both at 75 Hz) and off-resonance (acoustic drive at 50 Hz and spin-lock frequency at 75 Hz) images were acquired at 10 time points per block. The acquisitions were performed with the negative contrast version of the method, with the 90° flipback pulse along the x axis. The signal modulation is shown to be highest near the vibrating iron oxide sample. (d) Modulation response map of the block design experiment highlighting the location of the vibrating contrast agent sample, generated by voxel-wise statistical analysis of intensity changes between on- and off-resonance acquisitions. The highest z scores occur near the vibrating contrast agent source. Residual contrast appearing near the fluorinated oil sample is likely due to differences in turbulent motion between the two vibration settings which introduce different T_2* shortenings.

3.4.2 Effect Strength Characterization

The rotary saturation spectra in Fig. 3.3a demonstrate the AIRS effect as a function of both the iron oxide vibration frequency $\frac{\omega_{acoustic}}{2\pi}$ as well as the spin-lock frequency $\frac{\omega_{1lock}}{2\pi}$. For each

vibration frequency (blue curve = acoustic drive at 50 Hz, green curve = acoustic drive at 100 Hz, red curve = acoustic drive at 150 Hz, cyan curve = acoustic drive at 200 Hz), a rotary saturation spectrum is obtained by sweeping $\frac{\omega_{1lock}}{2\pi}$ through $\frac{\omega_{acoustic}}{2\pi}$. The scatter plots display measured data, which show that both the amplitude of the AIRS effect as well as its linewidth stay approximately constant across nanoparticle vibration frequency these observations are well-modeled by the Bloch simulation results which are plotted concurrently in the dashed-line curves.

Fig. 3.3b shows the strength of the AIRS effect increasing with higher nanoparticle vibration amplitude, consistent with the increased driving field $B_{rotarysat}$ derived from increased relative motions between the spin-locked water and the contrast agent B field source. Fig. 3.3c shows the increasing strength of the AIRS effect as sample Fe concentration increases, also due to the increased driving field $B_{rotarysat}$, which in this case is derived from higher susceptibility iron oxide solutions. The effect strength measured in tCNR is also shown in Fig. 3.3c, along with a linear fit of the data (R^2= 0.93) which intersects the tCNR = 1 dotted line at 20 μg/ml, indicating the method's sensitivity limit under the experimental conditions.

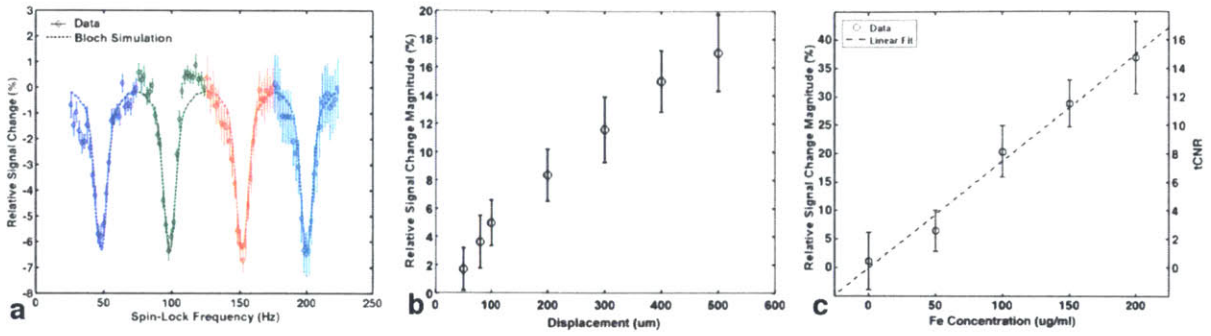

Fig. 3.3. (a) Characterization of the AIRS effect from the negative contrast version of the experiment as a function of spin-lock frequency with the acoustic drive of Fig. 3.2 set at each of 4 different frequencies (blue curve = acoustic drive at 50 Hz, green curve = acoustic drive at 100 Hz, red curve = acoustic drive at 150 Hz, cyan curve = acoustic drive at 200 Hz), with vibration displacement set to 150 μm and the sample concentration at 200 μg Fe/ml. Signal loss and the line-width of the resonance effect are approximately constant for the different iron oxide vibration frequencies. The solid curves are the Bloch equation simulation results using parameters based on the phantom (T_1 = 395 ms, T_2 = 316 ms, T_2* = 46 ms), and $B_{rotarysat}$ derived from a magnetic field perturbation model of a magnetized cylinder (14). (b) The magnitude of the relative signal change between on and off resonance conditions as a function of piezo actuator displacement (in the apparatus of Fig. 3.2) as measured by a laser Doppler vibrometer. The actuator vibration frequency was set to 50 Hz and spin-lock frequency was either 75 Hz (off-resonance state) or 50 Hz (on-resonance state), and the sample concentration was 200 μg Fe/ml. (c) Characterization of the AIRS effect (relative signal change magnitude between resonance states) in the apparatus of Fig. 3.2 as a function of iron concentration for a contrast agent vibration frequency of 50 Hz and spin-lock frequency set to either 75 Hz (off-resonance state) or 50 Hz (on-resonance state), and displacement was set to 500 μm. tCNR values as a function of Fe concentration shown alongside a linear fit with R^2= 0.93, which intersects with the dotted line (tCNR = 1) indicating a sensitivity limit of 20 μg/ml.

3.4.3 Positive contrast imaging and characterization

Fig. 3.4 shows positive contrast imaging of iron oxide nanoparticles using the AIRS method modified with a phase-shifted flipback pulse. In Fig. 3.4a, we observe the bright signal region unambiguously identifying the vibrating contrast agent sample. Both control samples and the background regions of the phantom exhibit nearly nonexistent signal. A modulation response map analysis of the on-resonance vs. no-vibration acquisition conditions is shown in Fig. 3.4b, demonstrating signal modulation only in the vicinity of the vibrating contrast agent sample. This effect can be observed in the timeseries signal intensity with the reference intensities subtracted

in Fig. 3.4c; the voxels near the vibrating iron oxide sample show a positive signal change during the on-resonance condition blocks. Even though the reference condition here is no-vibration instead of off-resonance as with the negative contrast experiments, because the absence of motion is effectively the same as being off-resonance in the spin-lock acquisition, the same basic phenomena is generated; this flexibility allows the reference condition to be chosen according to what is most convenient and practical for the experiment or scan session. Across the various concentrations of iron oxide samples tested, Fig. 3.4d. shows a nearly linear correlation between the positive contrast signal and Fe concentration, along with a linear fit of the data (R^2= 0.97).

3.5 Discussion

Our experiments demonstrate the feasibility of selectively imaging iron oxide contrast agents through a narrowband contrast modulation mechanism based on the rotary saturation effect. Separation of the agent's contrast from the background may enable quicker and more accurate visualization of injected MR iron oxide contrast agents in both research and clinical settings, particularly in acquisition scenarios with complex background contrast featuring multiple signal voids with various causes.

The characterization experiments show that signal change due to AIRS effect appears to be well-behaved across a number of physical parameters; of particular importance is its nearly linear correlation between effect intensity and iron oxide concentration in clinically relevant ranges, enabling not only simple visual evaluations of relative concentration levels, but also potentially the development of quantification techniques measuring contrast agent concentration.

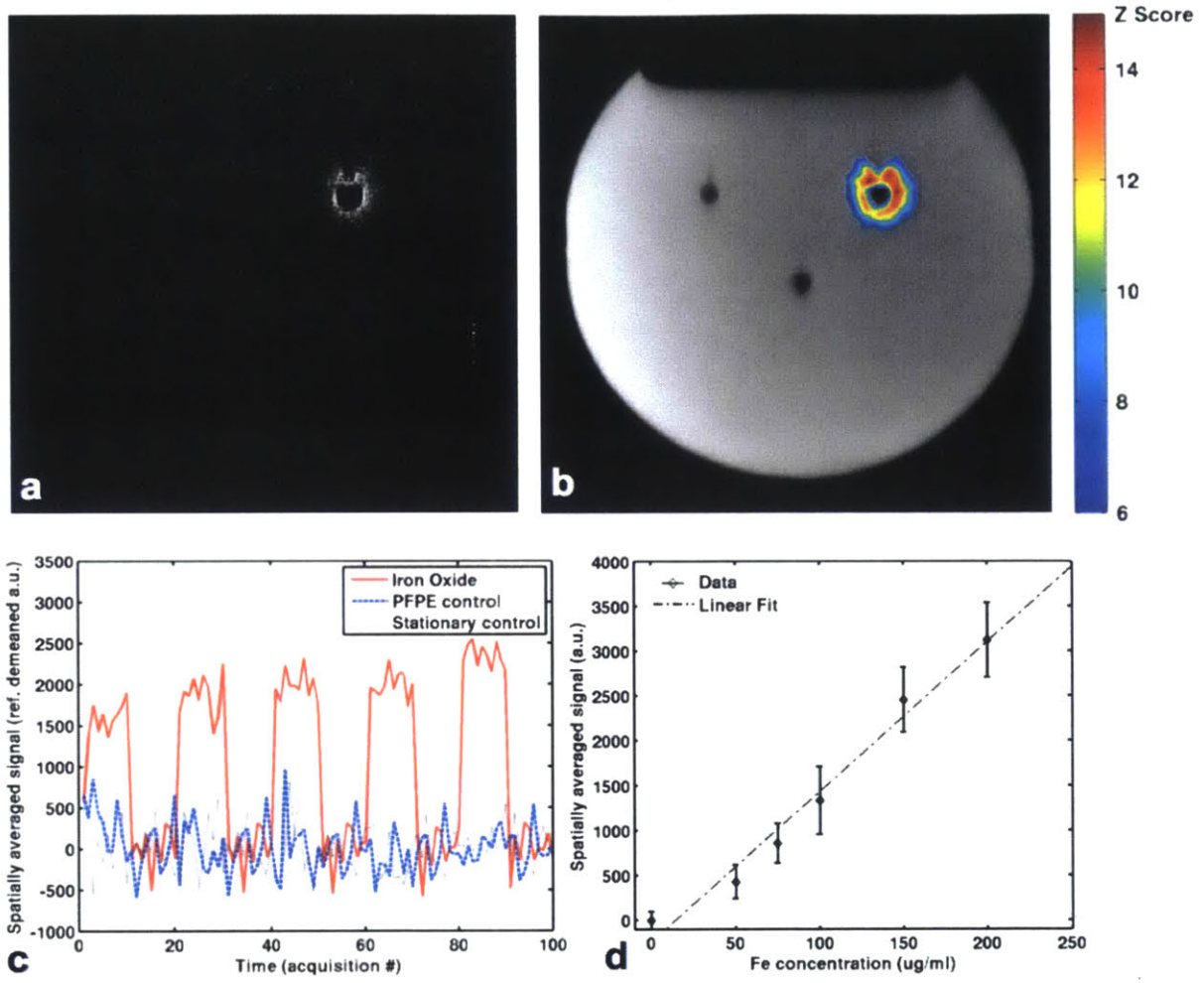

Fig. 3.4. Positive contrast imaging of iron oxide nanoparticles with the liquid phantom apparatus of Fig. 3.2a, by switching the 90° flipback pulse direction to be along the y axis. All experiments were conducted with the contrast agent vibration frequency at 75 Hz and spin-lock frequency set to 75 Hz. (a) Positive contrast image with 100 μg/ml Fe sample and spin-lock frequency 75 Hz (on-resonance). 100 acquisitions were taken, interleaving 10 on-resonance acquisitions and 10 no-vibration acquisition blocks. Each set of 50 acquisitions were averaged across time and the no-vibration average was subtracted from the on-resonance average to eliminate signal artifacts due to field inhomogeneity. (b) Modulation response map generated by statistical analysis of the signal difference between interleaved acquisition blocks. The highest z scores occur near the vibrating contrast agent source. (c) Time course of spatially averaged signal intensities near each sample over the experiment, demonstrating positive signal change during on-resonance acquisitions. (d) Spatially averaged positive contrast signal in the vicinity of the vibrating contrast agent sample increases with Fe concentration in a nearly linear fashion. The dashed line shows a linear fit of the signal data with R2= 0.97.

Although we have demonstrated a preliminary in-vitro validation of the technique here with a phantom setup established to primarily investigate the basic physical phenomena, our results indicate the AIRS contrast mechanism can be readily extended to tissue-mimicking gel phantoms

and in-vivo settings by the application of shear waves propagating through the sample media. The AIRS effect has been shown to effectively modulate contrast near the contrast agent with small vibration amplitudes in the tens of microns, the typical range of displacement amplitudes generated in shear waves through tissue during MR elastography with acoustic or piezoelectric drivers already used on patients during MR imaging [15,16].

In addition to addressing the problem of selective detection of contrast agents, techniques based on the AIRS mechanism may also be able to engage the recurrent goal in MR molecular imaging of improving the detection threshold for iron oxide nanoparticle agents. The instantly switchable contrast modulation ability in AIRS allows for hundreds of on-off cycles to be performed during acquisition, resulting in statistically boosted sensitivity in a manner similar to fMRI experiments, where signal changes less than 1% are routinely detectable. Based on our experiments, we demonstrated the sensitivity of our approach to be at least 20 Fe ug/ml for a 5-minute scan. This sensitivity is within the range of iron concentrations found in-vivo within tumors of animal studies, where typical biologically acceptable dosages of iron oxide nanoparticles between 10 and 100 mg Fe/kg (well below the mouse LD50 toxicity dose of 2000 mg Fe/kg [17]), result in iron oxide accumulations in various tumors at concentrations of 20-50 ug Fe/ml [18-20].

In comparison to several recently proposed "positive contrast" approaches with similar goals of selectively imaging iron oxide contrast agents, our method offers a different range of tradeoffs.

A potential limitation regarding the use of AIRS in-vivo is that with the proposed shear wave drive method, the entire tissue would tend to vibrate in bulk; thus, other sources of susceptibility difference (air, iron stores, etc...) within the vibrated tissue may also be picked up by¬ methods based on the AIRS effect. However, this limitation is not unique and should affect any imaging

method dependent upon the susceptibility properties of the iron oxide agents, including other positive contrast iron oxide imaging techniques.

Another reasonable concern regarding this property that shear waves tend to move connected tissue areas together is that the potentially reduced relative displacements may not generate the oscillating field strengths required for the AIRS method to be effective. However, focal lesions which would often be the target of these nanoparticle agents typically express mechanical properties significantly different from the surrounding background tissue. For example, hepatocellular carcinoma and focal nodular hyperplasia have vastly different shear stiffness than the normal liver tissue they are embedded in. [25] Propagating shear waves impinging upon the interface between these heterogeneous tissue regions face an acoustic impedance mismatch and thus would generate high relative displacement between tissue areas on the two sides of the interface with amplitude similar to that of the propagating wave [26-28]. As these shear wave amplitudes are typically delivered around 50-100 μm in-vivo, this places the relative displacement properties of the shear wave in tissue setup in a similar range as our piezoelectric actuator in the liquid phantom. Furthermore, for scenarios where there is reduced mechanical elastic coupling between the two tissue regions, (e.g. a fluid interface between the normal and pathological tissue), high relative displacement would also be expected across the interface.

This interface source of displacement also contributes to the expected effectiveness of the AIRS method for more complex geometries and various distributions of sizes of nanoparticle accumulations that would exist in-vivo. Additionally, as shown by Schenck [14], the geometry of the magnetic perturber affects the local B field distribution. For our experiments, we used both spherical and cylindrical samples - prototypical shapes representing two extremes of the

distribution of geometries a focal lesion (containing targeted nanoparticles) would exhibit, resulting in faster (1/r^3 for spherical) and slower (1/r^2 for cylindrical) ΔB field falloff. The success of our experiments demonstrates that the AIRS technique would work on a wide range of geometries and field falloffs. Regardless of the particular falloff rate or nanoparticle accumulation geometry, the AIRS phenomenon has been shown to be locally present with the nanoparticle sample and strongest near the center of the accumulation.

We also note that there is a possible "microscopic effect" not yet mimicked by our experiments for conditions in which relative motion at the nanometer scale between individual nanoparticles and local spin-locked water can generate the same AIRS contrast and manifest macroscopically in the image acquisitions. This is a potential research direction to further investigate and extend the AIRS effect.

Another challenge for in-vivo applications of the AIRS effect is the limitation to areas in the body where mechanical shear waves from the surface can penetrate to generate the tens of microns of displacement required for detection by the AIRS effect. Thus, tissue locations closer to the body's surface such as the liver and breast would be better suited than areas with less direct access, such as the heart. Additionally, even for tissues that have sufficient vibration amplitude, the potentially inhomogeneous propagation of shear waves within the tissue may negatively influence both relative and more quantifiable determinations of contrast agent concentration. However, this can be addressed by normalizing the effect according to measurements of the shear wave inhomogeneity, which can be acquired through MR elastography techniques.

The independence of the AIRS effect shown across a wide acoustic vibration frequency range eliminates the need to optimize vibration frequency on the acquisition side, allowing us to set the frequency to ensure sufficient penetration and propagation of shear waves in tissues of interest. MR Elastography experiments have demonstrated the appropriate range of driving frequencies for these tissues to be between 50 and 300 Hz [16]. These frequencies are well within the possible range for resonance with spin-locking fields.

A primary feature of the AIRS mechanism is the ability to rapidly induce contrast modulation with the iron oxide agents already present and thus shift the examination to an entirely post-injection paradigm, avoiding the long biological uptake time required by a typical pre- and post-injection comparison. As previously noted, scanner drift, subject motion, and other 1/f biological noise during this uptake time introduce confounding artifacts that currently make in-vivo automated detection methods impractical; by circumventing these limitations, we demonstrate the viability of automated mapping of contrast agents and potentially reduced uncertainty related to manual identification. Eliminating the need for pre-injection scans may also improve clinical throughput by obviating subsequent scan sessions or by reducing the extended durations of single sessions.

In this chapter we have introduced a novel contrast and contrast control mechanism to selectively image iron oxide contrast agents by modulating their contrast through a narrowband resonant spin-lock mechanism. Deploying this contrast mechanism in a block-design experiment which repeatedly cycles the effect of the agent on and off enables the removal of background contrast for sensitive and selective detection of the contrast agents via a statistically generated modulation response map. We demonstrate our method through validation experiments in phantoms, and we

show the strength of the AIRS effect to be generally well-behaved and robust across contrast agent concentration, displacement, and operating vibration frequency, indicating feasibility for its practical implementation in in-vivo settings.

The unique contrast modulation mechanism enables an entirely post-injection process that is quantitative in nature and robust against slow drifts in signal intensity due to scanner drifts and physiological motion. We also anticipate the method's clinical potential for reducing the conventional ambiguities associated with visualizing the presence of iron oxide contrast agents.

Bibliography

[1] Hahn MA, Singh AK, Sharma P, Brown SC, Moudgil BM. Nanoparticles as contrast agents for in-vivo bioimaging: current status and future perspectives. Analytical and Bioanalytical Chemistry 2011;399(1):3–27.

[2] Terreno E, Castelli DD, Viale A, Aime S. Challenges for molecular magnetic resonance imaging. Chemical Reviews 2010;110(5):3019–3042.

[3] Yoo D, Lee JH, Shin TH, Cheon J. Theranostic magnetic nanoparticles. Accounts of Chemical Research 2011;44(10):863–874.

[4] Rosen JE, Chan L, Shieh DB, Gu FX. Iron oxide nanoparticles for targeted cancer imaging and diagnostics. Nanomedicine : Nanotechnology, Biology, and Medicine 2012;8(3):275–290.

[5] Yu MK, Park J, Jon S. Targeting strategies for multifunctional nanoparticles in cancer imaging and therapy. Theranostics 2012;2(1):3–44.

[6] Mahmoudi M, Hosseinkhani H, Hosseinkhani M, Boutry S, Simchi A, Journeay WS, Subramani K, Laurent S. Magnetic resonance imaging tracking of stem cells in vivo using iron oxide nanoparticles as a tool for the advancement of clinical regenerative medicine. Chemical Reviews 2011;111(2):253–280.

[7] Taylor A, Wilson KM, Murray P, Fernig DG, Lévy R. Long-term tracking of cells using inorganic nanoparticles as contrast agents: are we there yet? Chemical Society Reviews 2012;41(7):2707–2717.

[8] Moriarty JM, Finn J P, Fonseca CG. Contrast agents used in cardiovascular magnetic resonance imaging: current issues and future directions. American Journal of Cardiovascular Drugs : drugs, devices, and other interventions 2010;10(4):227–237.

[9] Saeed M, Wendland MF, Higgins CB. Blood pool MR contrast agents for cardiovascular imaging. Journal of Magnetic Resonance Imaging: JMRI 2000;12(6):890–898.

[10] Abragam A. Principles of Nuclear Magnetism. Oxford: Oxford University Press; 1961. p 566-570.

[11] Redfield A. Nuclear Magnetic Resonance Saturation and Rotary Saturation in Solids. Physical Review 1955;98(6):1787 –1809.

[12] Witzel T, Lin FH, Rosen BR, Wald LL. Stimulus-induced Rotary Saturation (SIRS): a potential method for the detection of neuronal currents with MRI. NeuroImage 2008;42(4):1357–1365.

[13] Halpern-Manners NW, Bajaj VS, Teisseyre TZ, Pines A. Magnetic resonance imaging of oscillating electrical currents. Proceedings of the National Academy of Sciences 2010;107(19):8519-8524.

[14] Schenck JF. The role of magnetic susceptibility in magnetic resonance imaging: MRI magnetic compatibility of the first and second kinds. Medical Physics 1996;23(6):815–850.

[15] Muthupillai R, Lomas DJ, Rossman PJ, Greenleaf JF, Manduca A, Ehman RL. Magnetic

resonance elastography by direct visualization of propagating acoustic strain waves. *Science* 1995;269(5232):1854–1857.

[16] Mariappan YK, Glaser KJ, Ehman RL. Magnetic resonance elastography: a review. Clinical Anatomy 2010;23(5):497–511.

[17] O'Neil, MJ (ed.). The Merck Index – An Encyclopedia of Chemicals, Drugs, and Biologicals. 13th Edition. Whitehouse Station, NJ: Merck and Co., Inc.; 2001. p 519.

[18] Zhang J, Shin MC, Yang VC. Magnetic Targeting of Novel Heparinized Iron Oxide Nanoparticles Evaluated in a 9L-glioma Mouse Model. Pharm Res 2014:31(3):579-592.

[19] Choi GH, Seo SJ, Kim KH, Kim HT, Park SH, Lim JH, Kim JK. Photon Activated Therapy (PAT) using Monochromatic Synchrotron x-rays and Iron Oxide Nanoparticles in a Mouse Tumor Model. Radiation Oncology 2012:7:184.

[20] Seo SJ, Jeon JK, Jeong EJ, Chang WS, Choi GH, Kim JK. Enhancement of Tumor Regression by Coulomb Nanoradiator Effect in Proton Treatment of Iron-Oxide Nanoparticle-Loaded Orthotopic Rat Glioma Model. Journal of Cancer Therapy 2013:4(11):25-32.

[21] Cunningham CH, Arai T, Yang PC, McConnell MV, Pauly JM, Conolly SM. Positive contrast magnetic resonance imaging of cells labeled with magnetic nanoparticles. Magnetic Resonance in Medicine 2005;53(5):999–1005.

[22] Stuber M, Gilson WD, Schär M, Kedziorek DA, Hofmann LV, Shah S, Vonken EJ, Bulte JWM, Kraitchman DL. Positive contrast visualization of iron oxide-labeled stem cells using inversion-recovery with ON-resonant water suppression (IRON). Magnetic Resonance in Medicine 2007;58(5):1072–1077.

[23] Boada FE, Wiener E. Ultra-short echo time difference (USTED) data acquisition for T2* contrast reversal. Proceedings of the 14th Annual Meeting of ISMRM, Seattle, Washington, USA, 2006. p. 189.

[24] Girard OM, Du J, Agemy L, Sugahara KN, Kotamraju VR, Ruoslahti E, Bydder GM, Mattrey RF. Optimization of iron oxide nanoparticle detection using ultrashort echo time pulse sequences: comparison of T1, T2*, and synergistic T1- T2* contrast mechanisms. Magnetic Resonance in Medicine 2011;65(6):1649–1660.

[25] Yeh WC, Li PC,Jeng YM, Hsu HC, Kuo PL, Li ML, Yang PM, L PH. Elastic Modulus Measurements of Human Liver and Correlation with Pathology. Ultrasound in Med & Biol 2002:28(4):467-474.

[26] Zhou S, Robert JL, Fraser J, Shi Y, Xie H, Shamdasani V. Finite Element Modeling for Shear Wave Elastography. IEEE Ultrasonics Symposium, Orlando FL, USA, 2011, p. 2400-2403.

[27] Palmeri M, McAleavey S, Fong K, Trahey G, Nightingale K. Dynamic Mechanical Response of Elastic Spherical Inclusions to Impulsive Acoustic Radiation Force Excitation . IEEE Transactions on Ultrasonics, Ferroelectrics ,and Frequency Control 2006:53(11):2065-2079.

[28] Calle S, Remenieras JP, Hachemi ME, Patat F. Shear Wave Elastography: Modeling of the Shear Wave Propagation in Heterogeneous Tissue by Pseudospectral Method. IEEE Ultrasonics Symposium, Montreal, Canada, 2004, p. 24-27.

Chapter 4

Exploratory methods for Imaging Magnetic Nanoparticle Contrast Agents

In Chapter 3, we described the active contrast modulation paradigm as implemented by the Acoustically Induced Rotary Saturation (AIRS) technique, whereby the image contrast due to the nanoparticle contrast agents are modulated by an external acoustic stimulus. Here we describe two exploratory methods that expand upon this concept by modulating the contrast of contrast agents via 1) delivering audio-frequency oscillating magnetic fields (shifting B_0) and 2) probing the non-Gaussian field distributions experienced by water diffusing amongst nanoparticles.

4.1 Saturation Harmonic Induced Rotary Saturation

The Saturation Harmonic Induced Rotary Saturation (SHIRS) technique is also a modulate-able contrast mechanism that employs the spin-locking phenomena. However, since it requires only the application of an external oscillating magnetic field, it is potentially easier to apply than AIRS, which relies upon proper delivery of acoustic shear waves into tissue. The core of the mechanism is to exploit the magnetization-external field dependence of superparamagnetic iron oxide nanoparticles, whereby modulations of the externally applied B field concurrently changes the magnetization of the particles. If the frequency of the strong external field were set to $\gamma B1$lock, then a strong Rotary saturation effect would be seen. In this case it does not reflect the presence of the iron-oxide nanoparticles and is of little interest. But if we consider the non-linear response of the nanoparticles, we see that the particles will generate oscillating fields at harmonics of the applied field if they are driven into the saturation portion of their Langevin

curves, a phenomenon also exploited by Magnetic Particle Imaging but imaged by a different tomographic process unrelated to MRI [1].

4.1.1. Theory

The magnetization of an iron oxide nanoparticle contrast agent is governed by its magnetization-applied field (M-H) response curve, which is governed by the Langevin function (Eq 4.1). The superparamagnetism of these nanoparticles results in an M-H curve that is nonlinear due to their saturation behavior of the magnetization.

$$M(H) = n\mu L\left(\frac{\mu_0 H\mu}{k_B T}\right), \qquad \text{(Eq. 4.1)}$$

where H is the applied field, n is the number of nanoparticles in the sample, μ is the magnetic moment of each nanoparticle, μ_0 is the magnetic permeability of vacuum, k_B is the Boltzmann constant, T is the temperature, and L is the Langevin function $L(x) = 1/tanh(x) - 1/x$.

An time-varying oscillation of the applied field $H(t)$ around an operating point H_0 produces a time-varying oscillation in $M(t)$. Due to the nonlinearity of the M-H function, a sinusoidal $H(t)$ results in a distorted $M(t)$ function that has higher harmonics at multiples of the drive frequency, as illustrated in Fig. 4.1.

These higher frequency oscillations of $M(t)$ are experienced by the local water, which can be detected by spin-lock due to the rotary saturation effect in a similar manner to AIRS and SIRS [2,3,4]. By setting the resonant frequency of the spin-lock to a higher harmonic, we avoid saturating the signal by the drive field at the fundamental.

4.1.2 Preliminary validation experiment

A cylindrical phantom (8 cm diameter) was filled with a solution of Gadopentetate dimeglumine (Magnevist, Berlex Laboratories) yielding a T_1 measured by inversion recovery of 400 ms.

Aqueous samples of varying concentrations of 10 nm Fe_2O_3 nanoparticles (control: 25 μg Fe/ml, 50 μg Fe/ml, 100 μg Fe/ml, and 200 μg Fe/ml) were placed in 1 ml plastic centrifuge tubes and inserted into the cylindrical phantom. A custom-built Helmholtz coil powered by an audio amplifier, whose output was filtered by a passive notch filter tuned to eliminate second harmonic pickup by the receive coil, delivered spatially homogenous time-varying sinusoidal field shifts at 105 Hz.

A spin-lock prepared single-shot HASTE pulse sequence (Fig. 3.1b), similar to that of AIRS experiments previously described, was used in a 1.5T scanner (Siemens Avanto, Siemens Healthcare, Erlangen Germany) to capture images with 256x256 matrix, 10-cm FOV, 5mm slice thickness, TE of 14 ms, and TR of 3.0 s. The Helmholtz coil-delivered field oscillations are gated to be active only within the 100 ms spin-lock preparation sequence, during which the magnetization is manipulated due to the rotary saturation phenomenon and subsequently imaged with the HASTE readout.

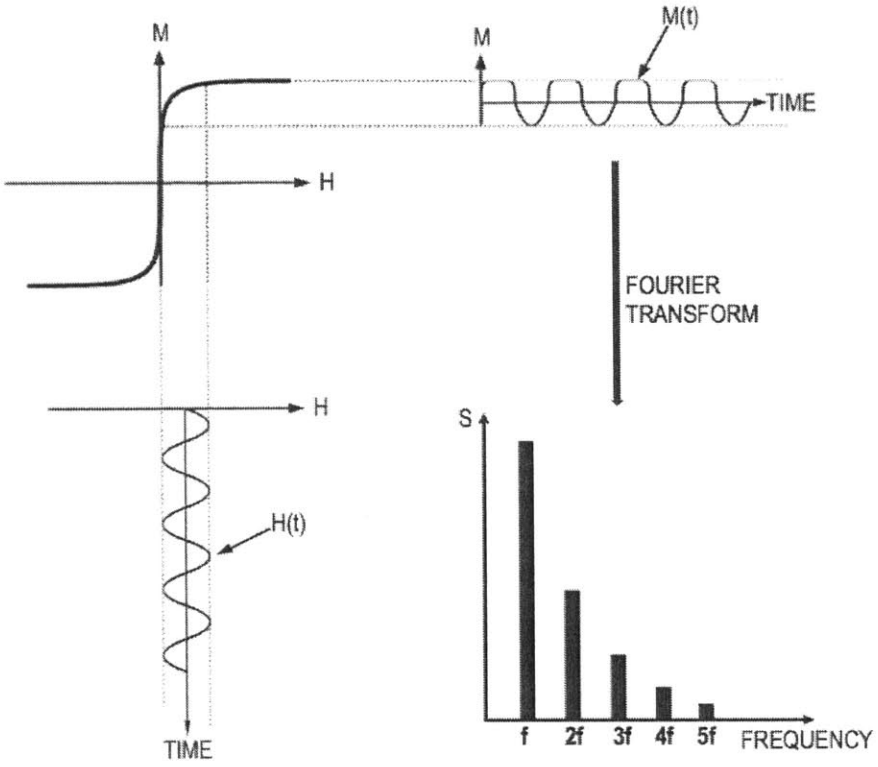

Fig. 4.1. Superparamagnetic magnetic nanoparticles experiencing a sinusoidally varying applied field $H(t)$ exhibit a distorted magnetization response $M(t)$ due to the nonlinearity of its M-H curve. The distortions introduce higher harmonics beyond the fundamental drive frequency f. The SHIRS method uses rotary saturation to detect the second harmonic oscillations to avoid picking up the drive field at the fundamental frequency.

A block design experiment was conducted by acquiring a set of 70 single-shot HASTE images while switching resonance states (on-resonance: $\omega_{1lock} = 2\omega_{drive}$, off-resonance $\omega_{1lock} \neq 2\omega_{drive}$) in 20 image blocks. In our experiment, $\frac{\omega_{drive}}{2\pi} = 105$ Hz, and $\frac{\omega_{1lock}}{2\pi}$ switched between 210 Hz and 190 Hz.

4.1.3 Preliminary validation results

Contrast modulation between on- and off-resonance conditions can be observed in voxels near iron oxide samples, particularly for the highest concentration sample. Fig. 4.2 shows representative on- and off-resonance HASTE spin-lock acquisitions.

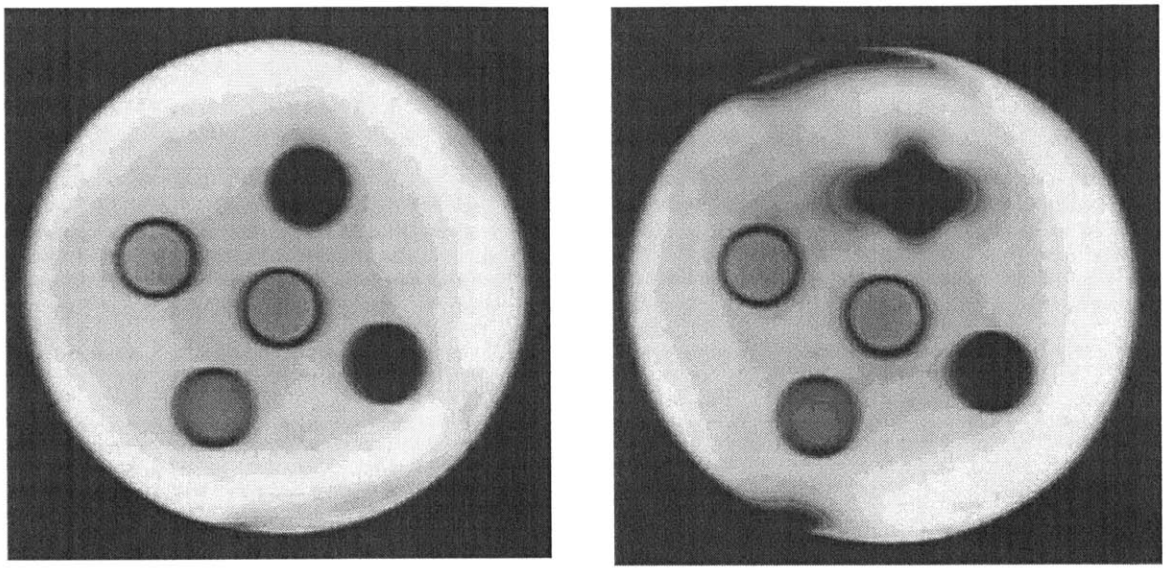

Fig. 4.2. Off resonance vs. on-resonance acquisitions in the presence of an oscillating drive field at 105 Hz, with spin-lock resonant frequency tuned off-resonance (left) to the 2nd harmonic, and on-resonance (right) at 210 Hz.

In Fig. 4.3, the time-series of an ROI placed around the highest concentration sample shows the relative signal change, which switches in accordance to the block design conditions of on- and off-resonance blocks of 10 images each. The time-series of an ROI around the control sample shows very little signal modulation across the block design experiment. This result is very similar to that from the AIRS experiment in Chapter 3, and shows promise for generating a similar fMRI-like "modulation response map." At this stage, our experiment requires refinement to eliminate artifacts that would confound such a sensitive quantitative analysis. We are in the process of improving the homogeneity of the Helmholtz coil-generated field, as well as the notch filter to further reduce second harmonic distortion from the power amplifier.

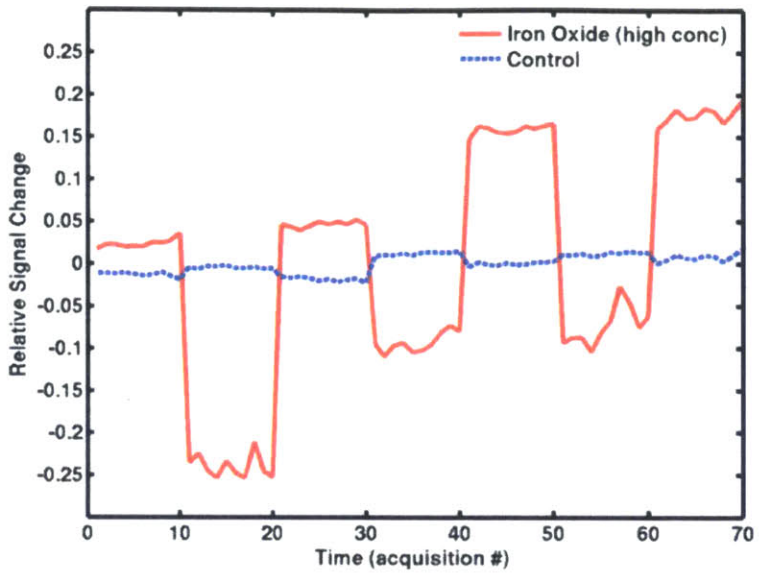

Fig. 4.3. Time course of voxel intensities near the control and high concentration iron oxide samples over the duration of the block-design experiment where interleaved blocks of on-resonance and off-resonance images were acquired at 10 time points per block. The acquisitions were performed with the negative contrast version of the method, with the 90° flipback pulse along the x axis.

4.2. Non-Gaussian Diffusion imaging of SPIO nanoparticles

Another method of generating contrast due to magnetic nanoparticle contrast agents we explore here is by probing the diffusion of water amongst the field perturbations generated by the nanoparticles. The diffusion signal of water in the presence of microscopic susceptibility variations due to iron oxide particles has conventionally been treated as Gaussian in nature [5,6]. However, even if the random walk of water motion is Gaussian, the highly nonlinear B fields and their gradients experienced by the water do not have a Gaussian distribution. We explore the potential for this property to be exploited as an MR contrast mechanism for detecting iron oxide contrast agents.

4.2.1. Theory and Background

A single magnetic nanoparticle perturbs the local magnetic field, approximated by that of a magnetized sphere, as described in [8]:

$$\Delta B_z = \frac{4\pi\Delta\chi B_0}{3}\left(\frac{a}{r}\right)^3\left(3\cos^2\theta - 1\right) = \frac{2x^2 + 2y^2 - 2z^2}{(x^2 + y^2 + z^2)^{5/2}} \qquad \text{(Eq. 4.2)}$$

The field gradient in the **z** direction can be thus calculated:

$$\frac{d\Delta B_z}{dz} = \frac{d}{dz}\left(\frac{2x^2 + 2y^2 - 2z^2}{(x^2 + y^2 + z^2)^{5/2}}\right) = \frac{3z(-4x^2 - 4y^2 + z^2)}{(x^2 + y^2 + z^2)^{7/2}} \qquad \text{(Eq. 4.3)}$$

How the pulsed gradient spin echo (PGSE) signal loss of a diffusing molecule behaves in the presence of a uniform background gradient G_0 was initially formulated by Stejskal & Tanner [9]:

$$\frac{S(G)}{S(0)} = \exp\left[-(\gamma\delta G)^2(\Delta - \delta/3)D\left(1 - \frac{TE - \Delta/2}{\delta G^2}\right)G \bullet G_0\right] = \exp\left[-bD - aG \bullet G_0\right] \qquad \text{(Eq. 4.4)}$$

The influence of a non-uniform gradient $\mathbf{G_0}$, such as that induced by a field of nanoparticles, can be approximated by considering its distribution $f(\mathbf{G_0})$ [5]:

$$\langle S(G)/S(0)\rangle = \int_{-\infty}^{\infty} f(G_0)\exp(-bD)\exp(-aG \bullet G_0)dG_0 \qquad \text{(Eq. 4.5)}$$

The distribution of these gradients due a field of nanoparticles for a diffusing water molecule are computed below in a Monte Carlo Simulation.

4.2.2 Monte Carlo Simulation

In order to examine the distribution of ΔB_z and $\frac{d\Delta B_z}{dz}$ a freely diffusing water molecule experiences in a field of iron oxide nanoparticles experiences, we performed Monte Carlo simulations of random walks.

First, we populated a three dimensional universe of randomly and uniformly distributed 10-nm diameter iron oxide (Fe_3O_4) nanoparticles with varying densities, and placed a proton at the center of the universe.

For every time step $\Delta t = 1x10^{-5}$ s until t = 100 ms (the length of a typical diffusion experiment), we simulated the stochastic diffusion of the proton by choosing a random displacement with mean 0 and standard deviation $\sqrt{2D\Delta t}$ where D is the diffusion coefficient in the three **x**, **y**, and **z** directions. We recorded the ΔB_z and $\frac{d\Delta B_z}{dz}$ the proton experienced at each time point, and repeated the simulation N=20,000 times. For each simulation, a separate random distribution of nanoparticles was populated.

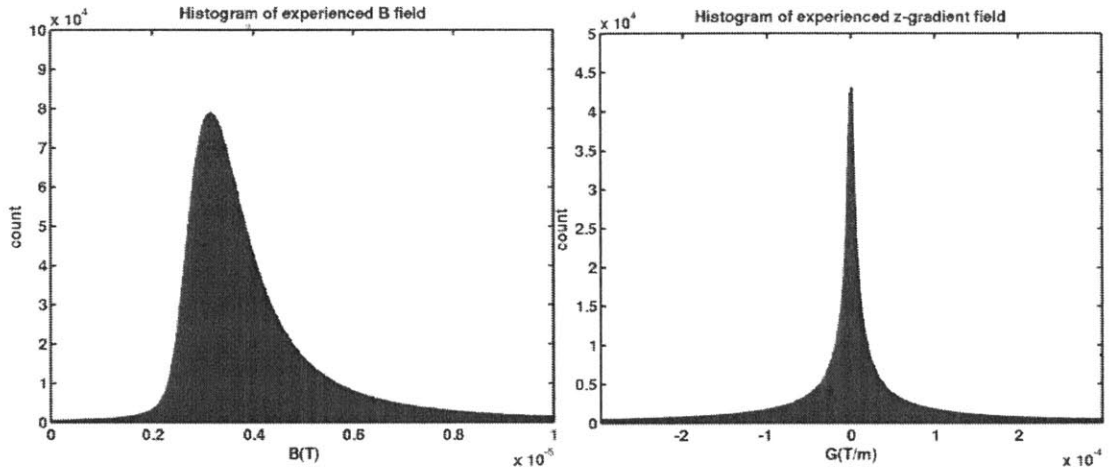

Fig. 4.4. Magnetic field and field gradient distributions for Monte Carlo simulation of diffusing water over a field of iron oxide nanoparticles of 5 μg Fe/ml concentration.

The results of this simulation are shown above in Fig. 4.4, for a 5 μg Fe/ml concentration. We observe that ΔB_z has a skewed distribution, and $\frac{d\Delta B_z}{dz}$ has characteristics of a peaked, kurtotic

distribution. This result is contrary to the conventional assumption of Gaussianity [5], which has been used in recent iron quantification experiments [6].

If we insert the gradient distribution into Eq. 4.5 above, we can obtain analytical insight into how the PGSE diffusion signal would behave in a nanoparticle solution as a function of b-value.

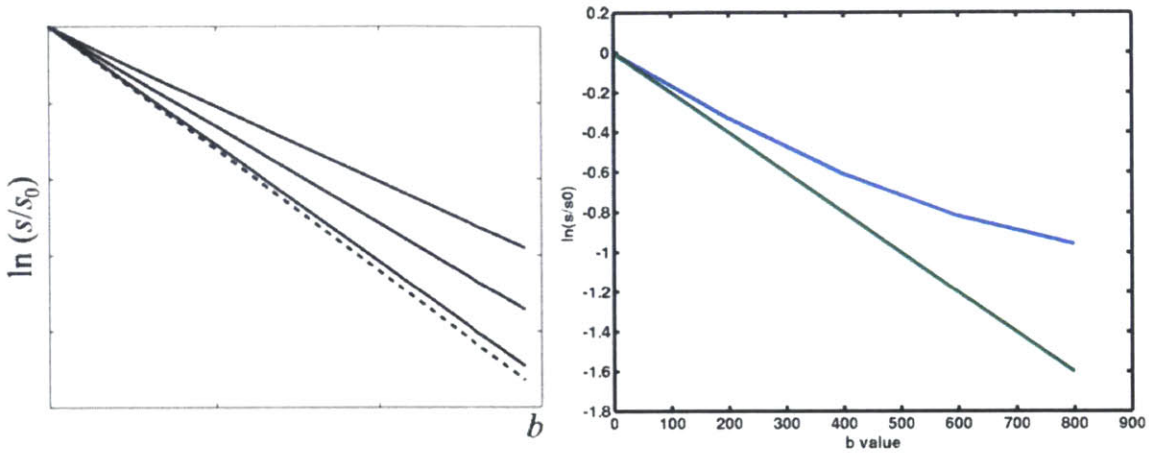

Fig. 4.5. Illustrations of log-signal loss vs. b-value curves obtained by Gaussian (left) or non-Gaussian kurtotic (right) distributions of field gradients across varying concentrations of nanoparticles. The kurtotic field distribution results in a nonlinear curvature of the signal loss profile, while Gaussian distributions maintain a linear profile and modify the apparent diffusion coefficient.

Fig. 4.5 demonstrates the differences in signal loss profiles Gaussian (left) and non-Gaussian kurtotic (right) distributions of field gradients. If the field gradients are assumed to have a Gaussian distribution $f(G_0) = \frac{1}{\sqrt{2\pi\sigma^2}} \exp\left(-\frac{G_0^2}{2\sigma^2}\right)$, where σ^2 represents the variance of the gradient fields, then Eq. 4.5 simplifies to

$$\langle S(G)/S(0) \rangle = \exp\left(-bD\left[1 - 0.5\gamma^2\Delta\sigma^2 D(TE - \Delta/2)^2\right]\right) \qquad \text{(Eq. 4.6)}$$

so that the log-signal loss profile is linear with respect to b-value. Higher nanoparticle concentration results in increased σ^2 and therefore a decreased apparent diffusion coefficient $D_{app} = D\left[1 - 0.5\gamma^2\Delta\sigma^2 D(TE - \Delta/2)^2\right]$, as demonstrated in the left graph of Figure 4.5, where

increasing nanoparticle concentrations result in decreasing-slope lines in the log-signal to b-value relationship. However, by inserting the field gradient distributions obtained by the Monte Carlo simulations, we observe a kurtotic effect where the signal loss profile becomes nonlinear and curves away from that of the control (green line) instead of a change in linear slope. We further investigated using this kurtosis difference to image iron oxide contrast agents in a phantom experiment.

4.2.3 Phantom validation experiment methods

A cylindrical phantom (8 cm diameter) was filled with a solution of Gadopentetate dimeglumine (Magnevist, Berlex Laboratories) yielding a T_1 measured by inversion recovery of 400 ms. Aqueous samples of varying concentrations of 10 nm Fe_2O_3 nanoparticles (control: 0 μg Fe/ml, 1 μg Fe/ml, 5 μg Fe/ml, and 10 μg Fe/ml) were placed in 1 ml plastic centrifuge tubes and inserted into the cylindrical phantom.

We used a PGSE diffusion pulse sequence on in a 1.5T scanner (Siemens Avanto, Siemens Healthcare, Erlangen Germany) to capture images with 128x128 matrix, 10-cm FOV, 5mm slice thickness, TE=100 ms, TR=1000 ms, with diffusion parameters δ = 15 ms, Δ = 40 ms, and increased the b value from 0 to 800 in increments of 200. 16 averages were taken per b-value. We further produced kurtosis maps from b0, b400, and b800 images, fitting to kurtosis values with the following expressions over each voxel:

$$K \approx 6\frac{D^{(12)} - D^{(13)}}{(b_3 - b_2)D^2} \qquad \text{(Eq. 4.7)}$$

where

$$D \approx \frac{(b_3 + b_1)D^{(12)} - (b_2 + b_1)D^{(13)}}{(b_3 - b_2)} \qquad \text{(Eq. 4.8)}$$

and

$$D^{(12)} \equiv \frac{\ln\left[\frac{S(b_1)}{S(b_2)}\right]}{(b_2 - b_1)}, D^{(13)} \equiv \frac{\ln\left[\frac{S(b_1)}{S(b_3)}\right]}{(b_3 - b_1)} \qquad \text{(Eq. 4.9)}$$

as described in [10]. In this instance, $b_1 = 0$, $b_2 = 400$, $b_3 = 800$.

4.2.3 Validation experiment results and discussion

The chart on the right shows the ROI-average signal loss profiles for each the iron oxide nanoparticle samples. Consistent with the Monte Carlo simulation results, we observe the curves deviating from a simple linear slope for the iron oxide samples, indicating kurtosis.

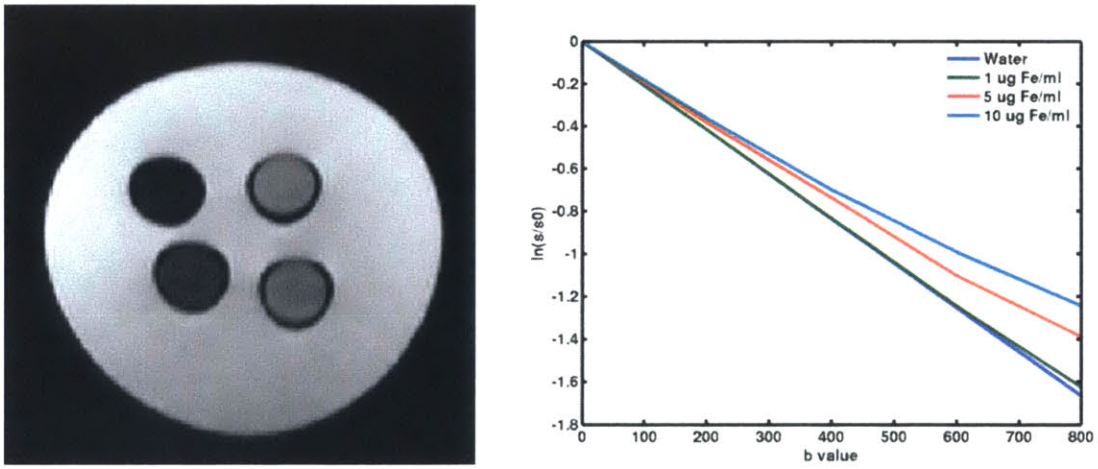

Figure 4.6. Conventional T2-image of liquid phantom containing varying concentrations of iron oxide samples (left), with concentrations increasing clockwise, starting from the upper-right sample. The log normalized signal for each sample is plotted against b-value (right). Increase in kurtotic curvature is observed with increased NP concentration.

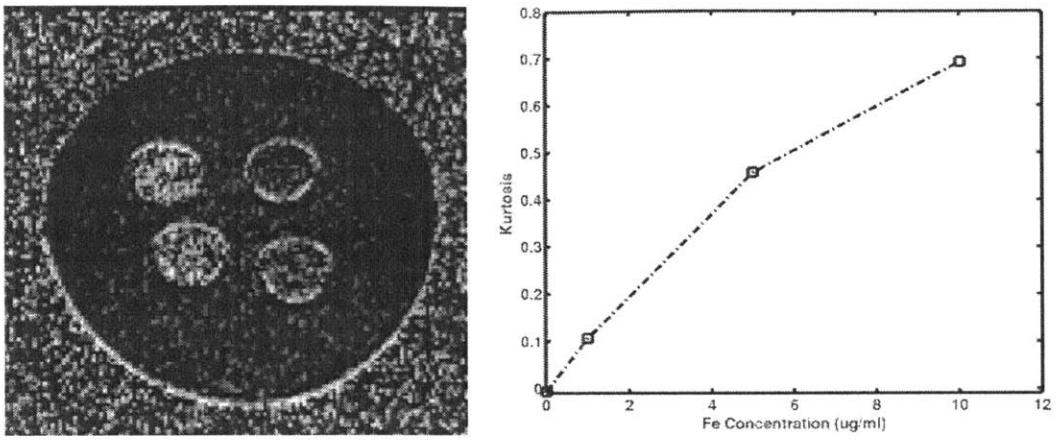

Figure 4.7. Grayscale kurtosis map shows iron oxide presence (left), and averaged kurtosis measure over the ROI of each sample is correlates well with iron oxide nanoparticle concentration (right).

The kurtosis was computed for each voxel according to Eqs. 4.7-4.9 and mapped in Figure 4.7 (left), which shows sensitivity to the location and concentration of iron oxide nanoparticles. By averaging the kurtosis values over a ROI for each sample, we see a clear correlation between the kurtosis value and iron concentration, suggesting a potential mechanism to quantify iron. This technique appears to be quite sensitive, even at 1μg Fe/ml concentration, which is near the lowest levels of iron concentration conventional T2* imaging is capable of. [11] In practice, such a quantification technique would require prior knowledge of the iron oxide nanoparticle used, in particular its size and magnetization properties, and at this stage, would also require Monte Carlo simulation. However, future work may reveal analytical or otherwise simple relationships that can accurately model how the kurtosis is expected to behave with the known nanoparticle properties and diffusion imaging parameters.

Bibliography

[1] Gleich B, Weizenecker J. Tomographic imaging using the nonlinear response of magnetic particles. Nature 2005;435:1214–1217. doi: 10.1038/nature03808.

[2] Zhu B, Witzel T, Jiang S, Huang S, Rosen B, Wald L. Selective magnetic resonance imaging of magnetic nanoparticles by acoustically induced rotary saturation. Magnet Reson Med 2016;75. doi: 10.1002/mrm.25522.

[3] Witzel T, Lin FH, Rosen BR, Wald LL. Stimulus-induced Rotary Saturation (SIRS): a potential method for the detection of neuronal currents with MRI. NeuroImage 2008;42(4):1357–1365.

[4] Redfield A. Nuclear Magnetic Resonance Saturation and Rotary Saturation in Solids. Physical Review 1955;98(6):1787 –1809.

[5] Zhong J., Kennan R., and Gore J, Effects of Susceptibility Variations on NMR Measurements of Diffusion, Journal of Magnetic Resonance 1991 95:267-280.

[6] Fujiwara S, Uhrig L, Amadon A, Jarraya B, Bihan LD. Quantification of iron in the non-human primate brain with diffusion-weighted magnetic resonance imaging. Neuroimage 2014.

[7] Einstein A. On the theory of the Brownian movement. Annalen der physic,1906;4:371–381.

[8] Schenck JF. The role of magnetic susceptibility in magnetic resonance imaging: MRI magnetic compatibility of the first and second kinds. Medical Physics 1996;23(6):815–850.

[9] Stejskal E and Tanner J, Spin Diffusion Measurements: Spin Echoes in the Presence of a Time-Dependent Field Gradient, Journal of Chemical Physics 1965 42:1:288-292.

[10] Jensen JH, Helpern JA. MRI quantification of non - Gaussian water diffusion by kurtosis analysis. NMR in Biomedicine, 2010. doi: 10.1002/nbm.1518.

[11] Dahnke H, Schaeffter T. Limits of detection of SPIO at 3.0 T using T2* relaxometry. Magn. Reson. Med. 2005;53:1202–1206.

Chapter 5

Summary

In this thesis we have demonstrated novel advantages of integrating acoustic and paramagnetic/superparamagnetic forms of exogenous MR contrast. We showed that for liver fibrosis evaluated in a DEN rat model, collagen-targeting paramagnetic probes and MR elastography, which are sensitive to different aspects of the disease, have complementary diagnostic and staging abilities. We showed that a composite score based on an optimized multivariate linear model was able to incorporate the discriminating capabilities of the separate techniques and thus have excellent accuracy in detecting both mild and advanced fibrosis. We then showed an even deeper integration of acoustics and molecular-targeting agents in the form of a novel contrast mechanism (AIRS) that could switch "on" and "off" the MR contrast due to the agents by modulating the frequency of acoustic/mechanical vibrations. This contrast modulation enables unambiguous location of the superparamagnetic agents as well as sensitive and quantitative statistical comparisons via fMRI-like modulation response map analysis of block design experiments. Promising results were shown for a variant of AIRS, Saturation Harmonic Induced Rotary Saturation (SHIRS), which replaced acoustic vibrations as the source of exogenous modulating energy with external B_0 oscillations that generated magnetization oscillations in the superparamagnetic nanoparticles, whose unique higher harmonics can be selectively detected by a spin-lock pulse sequence. Finally, an exploratory method of detecting iron oxides' non-Gaussian, kurtotically distributed field gradients by diffusion imaging was studied. While more work remains to be done to develop these techniques and indicate feasibility in more *in-vivo* settings, this thesis demonstrated promising new ways of utilizing

exogenous methods of modulating MR contrast to further extend the diagnostic flexibility of magnetic resonance imaging.